

Ulrike Plank

**Untersuchung der temperaturabhängigen Rückhaltung von in  
Wolframoberflächen implantiertem Stickstoff mittels  
Röntgenphotoelektronenspektroskopie**

**IPP 17/49  
Juni, 2016**

Ludwig-Maximilians-Universität München  
Fakultät für Physik

Masterarbeit

**Untersuchung der temperaturabhängigen  
Rückhaltung von in Wolframoberflächen  
implantiertem Stickstoff mittels  
Röntgenphotoelektronenspektroskopie**

von  
Ulrike Plank



Gutachter: PD Dr. Jörg Stober

Fassung vom 11.04.2016



# Kurzfassung

Zukünftige Fusionsreaktoren sollen in der Divertorkonfiguration betrieben werden, um die Fusionsenergie und Verunreinigungen möglichst effizient aus dem Fusionsplasma zu entfernen [1, 2]. Dabei sind die Divertorplatten einem hohen Teilchen- und Wärmefluss ausgesetzt. Um diesen Fluss zu reduzieren, wird absichtlich Stickstoff in die Plasmarandschicht eingebracht, da er durch Emission von Linienstrahlung das Randplasma kühlt [3]. Der ionisierte Stickstoff kann jedoch mit Wolfram, welches als Material für die Plasmawand verwendet wird, chemisch wechselwirken und es bildet sich Wolframnitrid in der Wandoberfläche. Dessen Bildung, sowie die Rückhaltung von Stickstoff in Wolfram, zeigten in früheren Experimenten ein unerwartetes Temperaturverhalten im Bereich 300 bis 800 K [4].

Aus diesem Grund wurde die Wolframnitridbildung und das Erosionsverhalten von Wolframnitrid unter Argonbeschuss in besagtem Temperaturbereich genauer studiert. In einem Laborexperiment wurden im Ultrahochvakuum energetische Stickstoffionen mit 300 eV in Wolfram implantiert. Dabei wurde die Entwicklung der Oberflächenzusammensetzung mittels Röntgenphotoelektronenspektroskopie untersucht. Anschließend wurde mithilfe von Argonionen das entstandene Wolframnitrid schichtweise erodiert, um die Verteilung des Stickstoffs in der Tiefe zu bestimmen.

Eine quantitative Analyse der gemessenen Spektren zeigt, dass die Wolframnitridphase bis 800 K thermisch stabil ist. Dagegen nimmt die Stickstoffkonzentration stark ab, wenn Stickstoff bei erhöhter Temperatur implantiert wird. Ein zur Oberfläche gerichteter Stickstoffverlust entsteht also erst bei gleichzeitiger Ionenbestrahlung. Die einfallenden Ionen erzeugen durch Schädigung der Kristallstruktur zusätzliche Defekte, die zu einer Mobilisierung des Stickstoffs führen. Dieser zusätzliche Verlustkanal kann auch die Beobachtung erklären, dass die Stickstofferosion durch Argonbeschuss bei erhöhter Temperatur erhöht ist. Die Aktivierungsenthalpie dieses Stickstoffverlusts wurde mithilfe der durchgeführten Messungen berechnet. Für den Beschuss mit 300 eV Stickstoffionen beträgt sie 0.082 eV und ist damit erheblich niedriger als die Aktivierungsenthalpie für thermische Diffusion von Stickstoff in Wolfram bei 900 K oder die Enthalpie, die für eine Leerstellenwanderung im Wolframkristall überwunden werden muss [5, 6]. Diese Prozesse alleine können den thermisch aktivierten Verlust von Stickstoff während des Ionenbeschusses daher nicht erklären.

# Abstract

Future fusion reactors will be operated in the divertor configuration, to allow an efficient particle and power exhaust [1, 2]. The divertor target plates are, however, exposed to a high power and particle load. To reduce the heat flux on them, nitrogen (N) is intentionally seeded into the edge plasma where it acts as a radiative coolant [3]. As a side effect, nitrogen interacts with the wall material tungsten (W) and forms tungsten nitride (WN) layers. Their formation and the N retention in W shows an unexpected temperature dependence in the temperature range from 300 to 800 K [4].

For this reason, the temperature dependence of the WN formation and its erosion was studied in laboratory experiments. N ions of 300 eV kinetic energy were implanted under ultra-high vacuum conditions into tungsten samples in the temperature range from 300 to 800 K. The composition evolution in the surface was observed by X-ray photoelectron spectroscopy. Sputter depth profiling, employing argon ions, was used to determine the depth distribution of the implanted nitrogen and the WN erosion under ion bombardment.

A quantitative analysis of the XPS spectra reveals that the WN phase is thermally stable up to 800 K. In contrast, the N concentration in the surface decreases significantly but gradually with increasing implantation temperature. This decrease is due to a N loss process to the surface which depends on both ion irradiation and temperature. Its occurrence can be explained by the bombardment induced creation of defects in the tungsten surface which mobilize the nitrogen atoms. This effect also accounts for the observation that the N erosion under argon bombardment is increased at elevated temperature. From the implantation measurements with the 300 eV N ions, the activation enthalpy for this temperature dependent loss process was calculated to 0.082 eV. It is significantly lower than the enthalpy for thermal diffusion in tungsten at 900 K or the vacancy migration enthalpy in tungsten [5, 6]. Therefore, these processes are not sufficient to explain the thermal activated N loss during ion bombardment.

# Contents

<b>1</b>	<b>Introduction</b>	<b>4</b>
<b>2</b>	<b>Interaction of Energetic Ions with Matter</b>	<b>9</b>
2.1	Reflection, Implantation and Sputtering . . . . .	9
2.2	SDTrimSP . . . . .	10
2.3	Diffusion . . . . .	12
<b>3</b>	<b>X-Ray Photoelectron Spectroscopy</b>	<b>15</b>
3.1	Physical Principle and Binding Energy Referencing . . . . .	15
3.2	Spectral Features . . . . .	16
3.3	Analysis Methods with XPS . . . . .	20
3.4	Instrumentation . . . . .	22
<b>4</b>	<b>Experimental Procedure</b>	<b>27</b>
4.1	Preparation of the XPS Device . . . . .	28
4.2	Evaluation of XPS Spectra . . . . .	29
4.3	Forward Calculation . . . . .	32
4.4	Fluence Calculation . . . . .	32
4.5	Characterization of the Ion Source . . . . .	33
<b>5</b>	<b>Results and Discussion</b>	<b>36</b>
5.1	Annealing after Implantation . . . . .	36
5.2	Implantation at Different Temperatures . . . . .	39
5.3	Erosion of Tungsten Nitride . . . . .	42
5.4	Activation Enthalpy Calculation . . . . .	44
<b>6</b>	<b>Conclusion</b>	<b>49</b>
6.1	Summary . . . . .	49
6.2	Outlook . . . . .	50
<b>A</b>	<b>Further Measurements</b>	<b>53</b>
A.1	Temperature Ramp . . . . .	53
A.2	Fluence Dependence . . . . .	54
	<b>Bibliography</b>	<b>55</b>

# Chapter 1

## Introduction

Werner Heisenberg, the co-founder of quantum mechanics, was also a moving force in nuclear fusion research in Germany. He supported the idea of using controlled nuclear fusion for energy production on Earth. At a university celebration in 1955, he formulated his motivation in the following way: “When we have achieved this goal, humans have fetched ‘the fire from the stars’ and the energy resources on Earth have become inexhaustible”<sup>1</sup>. For this purpose, he initiated the first research institute on nuclear fusion in Germany, the Max Planck Institute of Plasma Physics [7]. About 60 years have passed and scientists all over the world have done research on the field of nuclear fusion to realize this vision. The next pages give a short overview of the physical problems and the achievements to date in developing a nuclear fusion reactor.

To gain energy, our Sun fuses four protons to a  ${}^4\text{He}$  nucleus [8]. This reaction takes a long time, since the weak interaction is required for the conversion of protons to neutrons [2]. Physically speaking, the reaction parameter  $\langle\sigma v\rangle$  of this nuclear reaction is very low. An other fusion reaction has to be applied on Earth, one that has a higher reaction parameter. The most promising candidate is the fusion of deuterium (D) and tritium (T) to an alpha-particle ( ${}^4\text{He}$ ) and a neutron (n) under an energy release of 17.6 MeV per reaction:



This energy release, as well as the reaction parameter, are high compared to other possible fusion reactions (see figure 1.1).

To be close enough to undergo a fusion reaction, the reactants have to overcome the repelling Coulomb force between their positive charged nuclei. A temperature of

$$T \geq 10 \text{ keV}$$

is required<sup>2</sup> [2]. At such high temperature, the hydrogen particles are ionized and

---

<sup>1</sup>German Original: “[...] Wenn man dieses Ziel erreicht habe, dann hätten die Menschen wirklich das ‘Feuer von den Sternen’ geholt und die Energievorräte auf der Erde wären praktisch unerschöpflich geworden.” Quotation from [7].

<sup>2</sup>In nuclear fusion physics, it is common to give the temperature in the units of energy. The quantities are connected via the Boltzmann constant  $k_B$ :  $E_{\text{therm}} = k_B T$ . Hence, 10 keV correspond to a temperature of approximately 100 million K.

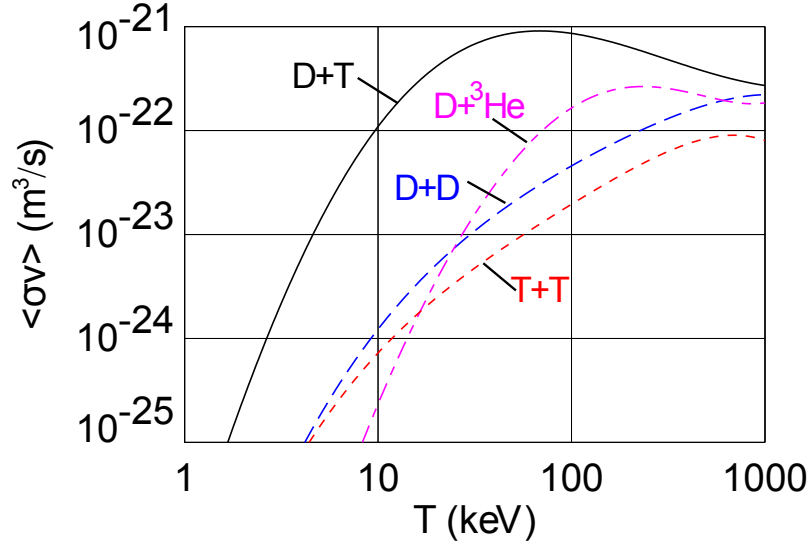


Figure 1.1: Reaction parameter against temperature for different fusion reactions. The D + T fusion overcomes the Coulomb barrier at comparably low temperatures. Hence, it is the best candidate to be used for nuclear fusion on Earth. Figure from [2].

form a plasma. Besides the plasma temperature, the plasma density  $n$  and the energy confinement time  $\tau_E$  are important for a self-sustaining nuclear fusion reaction. The fusion reactor reaches ignition when the Lawson criterion is fulfilled. This means, that the triple product  $nT\tau_E$  fulfills the condition:

$$nT\tau_E \geq 2.9 \times 10^{21} \text{ keV s m}^{-3}.$$

If this value is reached, there are enough nuclear fusion reactions to compensate all energy losses and therefore the plasma sustains fusion without external power input [2, 9].

In the Sun, the plasma particles are confined by gravitational forces which keep the nuclear reactions going. The number density of the fusion plasma is about  $10^{35} \text{ m}^{-3}$  [10], a value which is not attainable on Earth. Hence, two different approaches are followed to reach ignition. Inertial confinement fusion attempts to initiate nuclear fusion by heating a pellet of D-T fuel within a very short time to the required temperatures. Nuclear reactions can take place while the plasma is confined by its own mass inertia. The energy of the nuclear reactions in the center will then be used to heat the surrounding fuel and drive the chain reaction [2].

The second approach for plasma confinement is via a magnetic field, where the charged fuel particles follow the magnetic field lines. In the tokamak<sup>3</sup> configuration (see figure 1.2), the plasma is confined in an axisymmetric torus of toroidal field coils. The particles follow the emerging closed field lines but also drift to the outside of the torus since the magnetic field is higher on the inner side of the torus than on the outer side. A solenoid in the middle of the torus can compensate this drift by driving

<sup>3</sup>Russian acronym for “toroidal chamber with magnetic coils”.

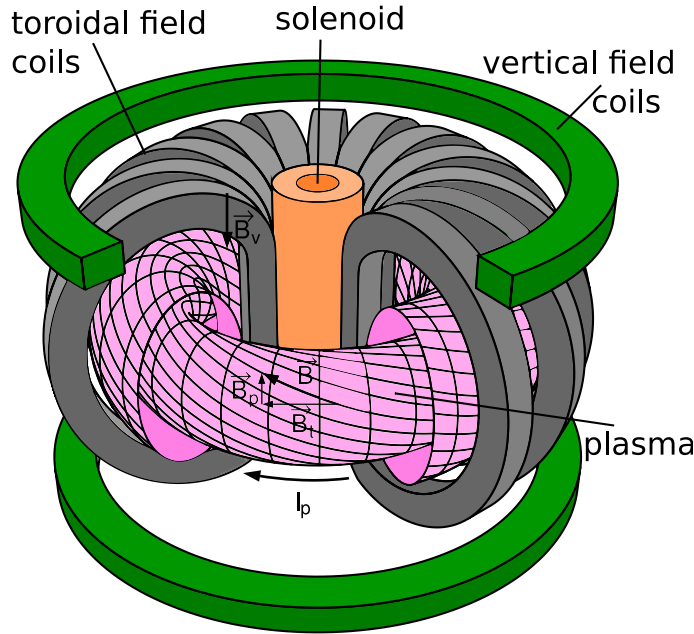


Figure 1.2: A schematic of a tokamak with the solenoid in the middle, producing a poloidal field, the toroidal magnets and two vertical field coils. The plasma particles are confined by following the closed twisted field lines. Figure adapted from [2].

a current through the plasma to build up a poloidal field. The resulting field lines are twisted and can be additionally adjusted by vertical field coils. An advantage of driving a current through the plasma is, that the current can also heat the plasma ohmically. The disadvantage is, that the plasma current can only be maintained for a limited time. Without additional heating, a tokamak can only work in a pulsed mode [2].

An alternative is the stellarator<sup>4</sup> configuration. The drift from the inner to the outer side is compensated by specially shaped electromagnets [2, 9]. This makes the construction and maintenance of a stellarator difficult. In both configurations, ignition can be maintained by using the emerging alpha-particles to heat the plasma by collisions with the deuterium fuel [2].

The confinement by magnetic field lines is not perfect, since a transport of particles and energy perpendicular to the magnetic field occurs, which is caused by hydrodynamic turbulence<sup>5</sup>. The plasma particles hit the surrounding wall material, interact and erode parts of the surface. These impurities as well as the moderated alpha-particles have to be removed from the plasma as they dilute it and cool it by radiative loss [2].

For this reason, future fusion devices will be operated in the divertor configuration. The inner plasma is separated by the separatrix from the outer plasma (the scrape off

<sup>4</sup>Here, the name comes from the Latin word “stella” which means star.

<sup>5</sup>For the description of the plasma, magnetohydrodynamics is employed and the plasma is referred to as a fluid [2].

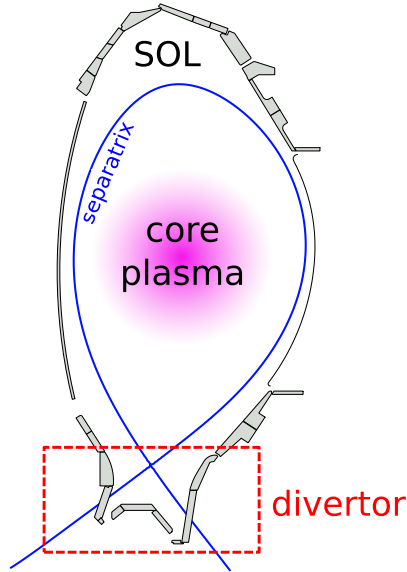


Figure 1.3: Cross section through a tokamak with divertor configuration. The separatrix (blue) isolates the core plasma (magenta) from the scrape-off layer (SOL) and intersects the wall at the divertor.

layer, SOL) in this configuration. While the inner field lines are closed and guarantee confinement, the separatrix and outer field lines intersect with the wall. They lead the impurities to specially designed target plates that are remote from the main plasma, the so called divertor (see figure 1.3) [2, 11, 12].

A suitable material for the divertor target plates is tungsten (W), since its erosion by impinging particles is very low [11]. As a divertor material, it has to withstand high thermal loads originating from the intense particle flux arriving into the divertor. To reduce the heat flux on the divertor plates, nitrogen (N) impurities are intentionally seeded into the plasma in the divertor region (see figure 1.4). In the SOL, N is not fully ionized, thus it can emit line radiation and therefore works as a coolant [3].

The ionized nitrogen is also accelerated to the divertor target plates and gets implanted into tungsten. The formed tungsten nitrides (WN) change the thermal and erosion properties of the wall material. Hence, they lead to an altered impurity content in the main plasma [12]. In particular, the temperature dependence of the WN phases is not fully understood and its investigation led to contradictory results [4, 14]. To improve our understanding of the WN formation, its temperature dependence and the WN erosion, this thesis was written.

In a laboratory experiment, nitrogen ions were implanted into a tungsten sample. A UHV system, equipped with two ion sources and the components for X-ray photoelectron spectroscopy (XPS), was employed for the in-situ implantation and for argon sputter depth profiles. The N accumulation and retention in W as well as the erosion of WN under argon bombardment was studied by XPS. The results and their discussion are presented in chapter 5. The performance of the measurements is described in chapter 4, the experimental method in chapter 3. Chapter 2 introduces the most important concepts occurring in ion interaction with matter and their

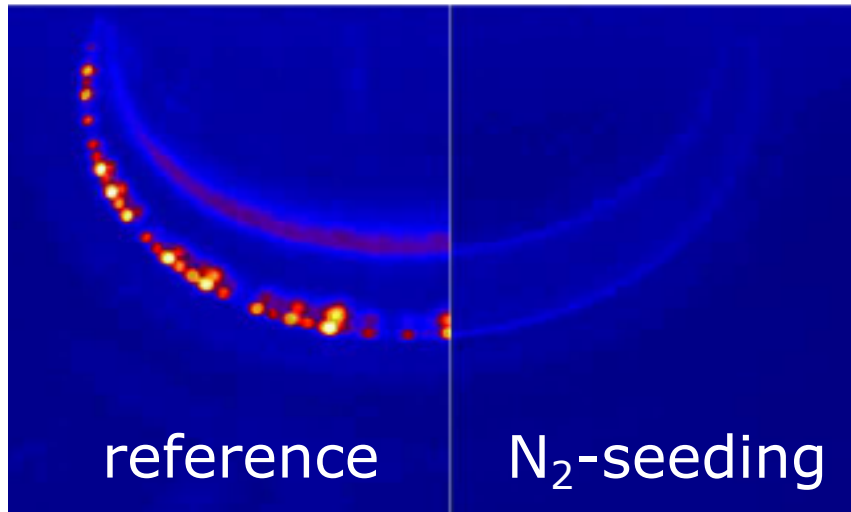


Figure 1.4: Thermal surface radiation of the divertor in the tokamak ASDEX Upgrade during a plasma discharge. On the reference picture, red spots are visible which indicate a hot surface caused by a high thermal load (left side). On the right side, a picture of the divertor during a discharge under same conditions but with nitrogen seeding is shown. The nitrogen reduces the heat load on the divertor by radiatively cooling the edge plasma. Figure from [13].

simulation. The conclusion (chapter 6) gives a short summary of the performed work and an outlook on possible future experiments.

# Chapter 2

## Interaction of Energetic Ions with Matter

Energetic particles impinging on a target undergo collisions with the target atoms. In the binary collision approximation, only collisions between two partners, the projectile and the target atom, are considered. The particle trajectory is described as a series of successive, independent binary collisions. In between two collisions, the particle travels straight a distance of the mean free path length  $\lambda_{\text{mfp}}$ . Electronic interactions are included as an energy loss process [14]. Chemical processes and diffusion are not taken into account, but play an important role in the retention of nitrogen in tungsten. They are described separately.

### 2.1 Reflection, Implantation and Sputtering

When particles in an ion beam collide with a target, a fraction of them gets backscattered from the target's surface (reflection). The remaining ions penetrate into the sample and undergo elastic collisions with the bound target atoms (nuclear energy loss) and inelastic collisions with the electrons (electronic energy loss). The nuclear collisions change the propagation of the penetrating particles. These can be directed back and leave the surface, if they still have enough kinetic energy to overcome the attractive surface binding energy (SBE). The fraction of backscattered particles depends on their energy and the angle of incidence. The penetrating particles can also lose their energy gradually and get implanted into the sample. The implantation depth depends on the initial energy of the particle [14, 15]. For N ions with an incident energy smaller than 10 keV, this is in the range of a few nanometers. The nuclear energy transfer leads to energetic target atoms which can themselves undergo collisions. A collision cascade is created and the target atoms which have enough energy, leave the sample (physical sputtering) [14]. Figure 2.1 illustrates the three effects taken into account in the binary collision approximation.

Physical sputtering depends on various parameters, namely the mass ratio of the target atoms and the projectiles, the initial energy of the projectile and its incident angle. A measure for sputtering is given by the sputter yield  $Y_{\text{sp}}$ . It is the number

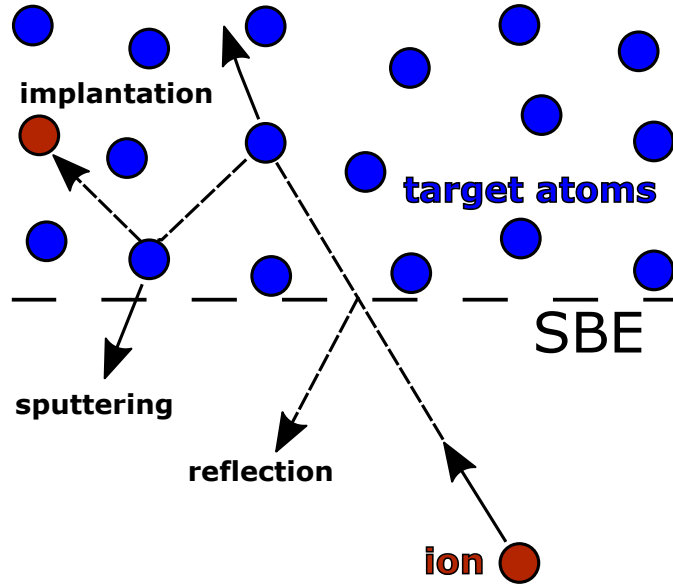


Figure 2.1: The interaction of energetic ions with matter can be described by the binary collision approximation. The collisions are supposed to be independent and the particle travels straight in between two collisions. Processes like reflection, implantation and sputtering can be described by this approximation. Figure adapted from [12].

of sputtered target atoms to the number of incident particles [14]. In the case of a system with different elemental components, only partial sputter yields can be calculated. The partial sputter yield is proportional to the abundance of the element in the surface. Since sputtering depends on the mass ratio, preferential sputtering of one component and relative enrichment of the remaining constituents in the surface can occur, which again influences the sputter yield [15].

The reflection yield  $Y_{\text{ref}}$  is defined in a similar way as  $Y_{\text{sp}}$ . It is the number of reflected particles to the number of incoming particles [14]. If

$$Y_{\text{sp}} + Y_{\text{ref}} < 1$$

for an ion type, then the remaining ions get implanted into the sample. From their implantation site, they can be transported deeper into the target or back to the surface via diffusive processes [12].

## 2.2 SDTrimSP

SDTrimSP is a Monte Carlo code which simulates the interaction of energetic particles with matter. To this purpose, it uses the binary collision approximation. For each collision, quantities like the path traveled between two collisions are drawn randomly from a distribution, determined by the atomic density of the material [16]. The collisions are assumed to be independent of each other and only repulsive interactions are included. Hence, the simulations are only valid for projectile energies of 50 eV or

higher [4, 14]. The modeled target consists of one dimensional layers with an infinite lateral size and an amorphous, randomized structure at zero temperature [16].

SDTrimSP can be operated in two modes: In the static mode, the target composition is fixed and reflection coefficients, implantation profiles and sputtering yields are calculated. In the dynamic mode, the target composition changes dynamically due to implantation and erosion. The latter is used to determine the depth distribution of implanted atoms [12, 16]. Chemical interactions are not included in the code but two values can be adjusted to take them into account: the surface binding energy and the maximum concentration of a given species. The SBE considers the attractive forces of a crystal lattice which make it more difficult for a particle to leave the target. With the maximum concentration, different chemical phases of interacting elements are taken into account.

The nitrogen depth distribution shown in figure 2.2 was simulated by Olaf Encke [10]. The dynamical mode of SDTrimSP version 5.00 was used for it. In the simulations, it was assumed, that N ions of 300 eV kinetic energy hit the W target<sup>6</sup> under an angle of 45°. The surface binding energy was set to 0.1 eV and the maximum N concentration to 0.5.

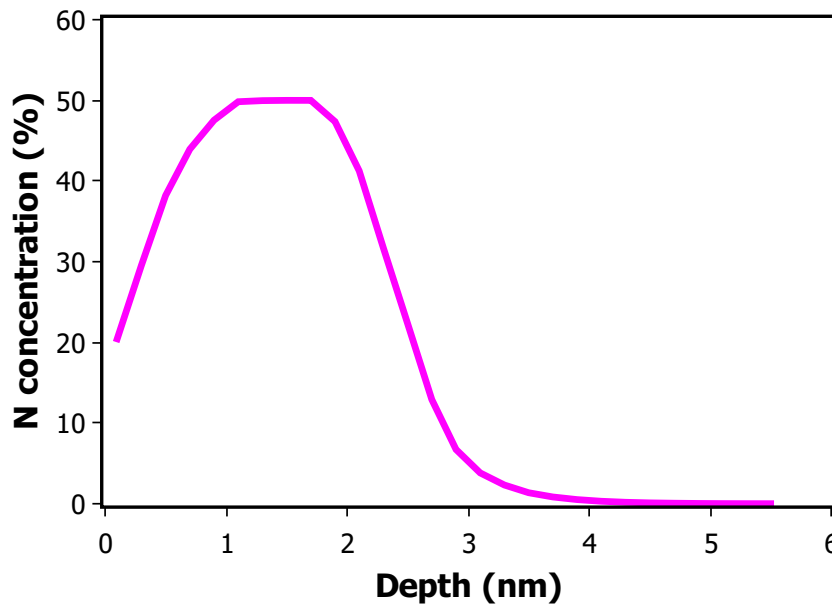


Figure 2.2: Nitrogen depth distribution obtained from the SDTrimSP simulation. It was assumed that N ions of 300 eV kinetic energy hit a W target. The maximum N concentration was artificially set to 50 % [10]. Figure from [17].

<sup>6</sup>Although tungsten has a crystal structure, the SDTrimSP code, which assumes an amorphous target structure, can be used. By ion bombardment, the crystalline structure will be locally disturbed which leads to amorphization of the target. Furthermore, the impinging ions could "see" an amorphous structure, depending on the orientation of the target towards the ion beam.

## 2.3 Diffusion

In a system with local concentration differences, particles move towards concentration minima until the concentration difference is balanced. This process is called diffusion and can be described by the random movement of the particles which leads to a net flux from the high concentration region to the low concentration region [2]. Diffusion appears in every physical phase of matter, but it is slowest for solids, since the atoms are strongly bound to their lattice sites. An empirical description for diffusion was given by Adolf Fick [18].

### Fick's Law

The first Fick's law,

$$\mathbf{\Gamma} = -D\nabla c, \quad (2.1)$$

connects the particle flux  $\mathbf{\Gamma}$  with the gradient of the concentration  $c$ . The proportionality constant  $D$  is called diffusion coefficient and has the dimension area per time ( $\frac{m^2}{s}$ ). The minus sign in equation (2.1) indicates, that the diffusion direction is opposite to the concentration gradient and it therefore reduces differences in concentration [2, 18].

In many cases, particle flux and concentration gradient are time- and location-dependent. Hence,  $D$  is determined by Fick's second law

$$\frac{\partial c}{\partial t} = \nabla \cdot (D\nabla c). \quad (2.2)$$

This partial differential equation results from inserting Fick's first law into the continuity equation

$$\frac{\partial c}{\partial t} = -\nabla \cdot \mathbf{\Gamma}. \quad (2.3)$$

The continuity equation formulates a conservation law. In a diffusion process, the number of diffusing particles is conserved. If the diffusion coefficient is independent of the location, equation (2.2) can be simplified to

$$\frac{\partial c}{\partial t} = D\Delta c, \quad (2.4)$$

with  $\Delta$  being the Laplace operator [2]. An analytical solution for the diffusion coefficient can only be given if  $D$  is constant. This is often the case for impurity atoms diffusing in metals [18].

### Diffusion in Metals

The fundamental process in metals is the diffusion of metal atoms. It is referred to as self-diffusion [19]. This, however, means, that atoms have to change their lattice sites. Therefore, crystal defects are required, in the case of self-diffusion, vacancies. Vacancies are unoccupied lattice sites which are present in every metal. Their production depends exponentially on the vacancy formation enthalpy  $H_f^V$ , and

their migration on the vacancy migration enthalpy  $H_m^v$ . To monitor self-diffusion, radioactive or stable isotopes of the investigated element (tracers) are used. The tracer self-diffusion shows, that the temperature dependence of diffusion follows in most cases a single Arrhenius relation [19]:

$$D = D_0 e^{-\frac{\Delta H}{k_B T}}, \quad (2.5)$$

where  $D_0$  is the pre-exponential factor which depends on the geometry of the system and it includes the defect-formation term.  $\Delta H$  is the activation enthalpy. For self-diffusion, it is the sum of  $H_f^v$  and  $H_m^v$ .  $D_0$  and  $\Delta H$  can be determined, when  $D$  is measured as a function of  $T$ . In the Arrhenius plot, the logarithm of  $D$  is plotted against the inverse of temperature. The y-intercept equals  $\ln D_0$  and  $-\frac{\Delta H}{k_B}$  is the slope of the curve [14, 18, 19].

Diffusion in substitutional alloys is more complicated because two kinds of diffusion occur. The solvent diffusion is the self-diffusion of the atoms building up the crystal lattice. The component which substitutes a fraction of the crystal atoms is called solute and its diffusion is referred to as solute diffusion. If the concentration of the solute is less than 1 %, then the diffusion is called impurity diffusion. Both the self-diffusion of the solvent and the impurity diffusion are driven by vacancy migration. Impurity diffusion also follows the Arrhenius relation.  $D_0$  and  $\Delta H$  for impurity diffusion, however, have to be corrected by several factors compared to self-diffusion [19].

Solutes which are smaller than the atoms of the metal do not occupy the lattice sites but the interstices of the lattice. The shape and the size of the interstitial sites are defined by the lattice geometry. The metal tungsten has a body centered cubic (bcc) structure with 6 octahedral and 12 tetrahedral sites per unit cell. The N ions populate these sites and jump from one interstitial to the next. For this diffusion process, the Arrhenius equation holds as well, but no defect-formation term enters the expression of  $D_0$ . It solely depends on geometry factors. The activation energy  $\Delta H$  is expressed by the interstitial migration enthalpy  $H_m^i$  [19].

## Radiation Enhanced Diffusion

The diffusivity in solids can be enhanced by ion irradiation. The impinging ions create vacancy-interstitial pairs in the metal. These additionally produced defects can be lost by recombination or in a defect sink, for instance dislocations of lattice atoms. The vacancy and self-interstitial concentrations,  $c_v$  and  $c_i$ , are determined by the competing production and loss processes [20]. Under the assumption that the thermal activation enthalpy of defect migration is not affected by the ion irradiation process, the radiation-enhanced-diffusion coefficient  $D_{\text{RED}}$  can be calculated accordingly [20, 21]:

$$D_{\text{RED}} = c_v D_v + c_i D_i. \quad (2.6)$$

$D_v$  is the vacancy diffusion coefficient and it is given by equation (2.5) for self-diffusion.  $D_i$  is the interstitial diffusion coefficient which is, except for self-diffusion, larger than  $D_v$ , because  $H_m^i$  is less than  $H_m^v$  [20]. Since the vacancy concentration under

irradiation is larger than in thermal equilibrium, the radiation-enhanced diffusion coefficient is larger than the thermal diffusion coefficient [21].

# Chapter 3

## X-Ray Photoelectron Spectroscopy

X-ray photoelectron spectroscopy (XPS) is a spectroscopy method which is based on the photoelectric effect. If a sample is irradiated by light of sufficient energy, electrons are emitted. The kinetic energy of these so-called photoelectrons depends on their binding energy and the energy of the incoming light. Albert Einstein could explain this phenomenon in 1905 by employing the photon, the energy quantum of light [22].

### 3.1 Physical Principle and Binding Energy Referencing

When a photon of energy  $E_{\text{photon}} = h\nu$  hits an atom in the target, it gets absorbed by an electron. The electron can leave the sample if the transferred energy is higher than the binding energy  $E_{\text{B}}^{\text{F}}$  of the electron and the work function  $\Phi_{\text{s}}$  of the sample. Its kinetic energy  $E'_{\text{kin}}$  is the excess energy from this absorption process:

$$E'_{\text{kin}} = h\nu - E_{\text{B}}^{\text{F}} - \Phi_{\text{s}}. \quad (3.1)$$

To measure the kinetic energy of the photoelectrons, the sample is placed in electrical contact with the spectrometer. This adjusts the Fermi levels of both the sample and the spectrometer to one common value. The work function of the spectrometer,  $\Phi_{\text{spec}}$ , is determined by calibrating the spectrometer. It measures the kinetic energy of the photoelectrons according to:

$$E_{\text{kin}} = E'_{\text{kin}} - (\Phi_{\text{spec}} - \Phi_{\text{s}}). \quad (3.2)$$

Since the energy of the incoming photon is known, the electron's binding energy can be calculated from these quantities (see also figure 3.1) [23]:

$$E_{\text{B}}^{\text{F}} = h\nu - E_{\text{kin}} - \Phi_{\text{spec}}. \quad (3.3)$$

In XPS, X-rays irradiate the sample. Their energy is appropriate to produce photoelectrons from the inner shells of the atom. The binding energies of the core

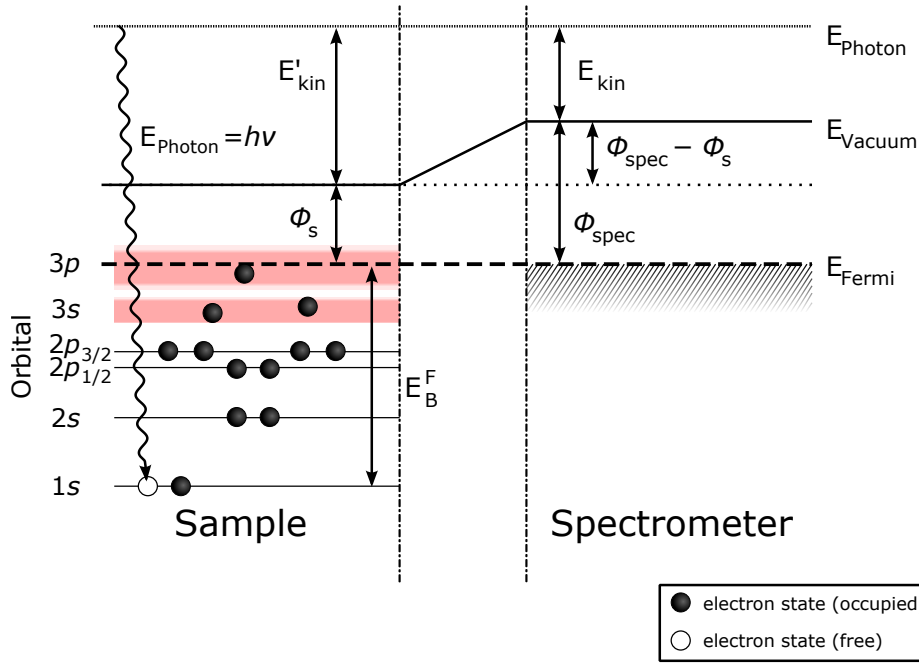


Figure 3.1: Relevant energy levels for XPS binding energy measurements. Figure adapted from [24].

electrons are characteristic for the particular element. Hence, the surface composition<sup>7</sup> can be studied by XPS.

A typical XPS spectrum plots the number of detected photoelectrons (as counts or counts per second) against their binding energy. The binding energy is plotted on the abscissa with increasing binding energy from the right to the left. Spectra reaching over a wide range (from 0 eV to approximately 1000 eV) are known as survey spectra. Figure 3.2 shows the survey spectrum for a WN sample. For detailed analysis of selected peaks and to reduce the acquisition time, short range spectra are acquired [23, 25].

## 3.2 Spectral Features

In figure 3.2, typical spectral features of an XPS spectrum are shown. The background is generally increased on the high binding energy side of the photoelectron peaks. This accumulation is attributed to photoelectrons which lose energy on their way out of the sample due to inelastic collisions [23, 25].

<sup>7</sup>To be detected, the photoelectrons have to leave the solid undisturbed. However, the inelastic mean free path of the photoelectrons in the sample is in the nm range. The information depth of XPS is therefore only a few nanometers. See also section 3.3

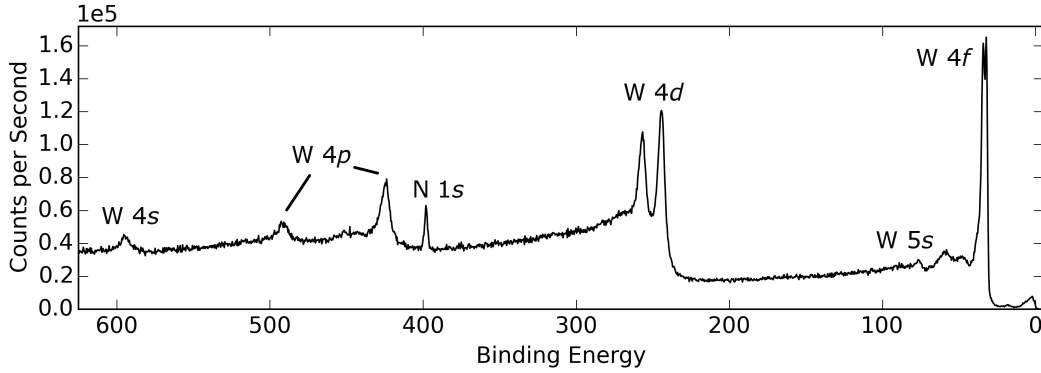


Figure 3.2: Typical XPS survey spectrum of a WN sample irradiated by a monochromatic Al source: Abscissa with increasing binding energy from the right to the left; Ordinate with peak intensity in counts per second.

### Origin and Shape of the Peaks

Single peaks originate from s-orbitals where  $l = 0$  (e.g. the W 4s and W 5s peak in the spectrum) [25]. The photoelectron peaks related to an angular momentum quantum number  $l \neq 0$  appear as doublet in the spectrum (W 4f, W 4d and W 4p). This splitting originates from the spin-orbit coupling. The spin of the photoelectron can either be parallel or anti-parallel to the angular momentum. This can be also seen by introducing the total angular momentum quantum number  $j$ , which is calculated via

$$j = |l + s|, \quad (3.4)$$

with  $s = \pm 1/2$ , the spin quantum number. For a non-vanishing angular momentum  $l$ , this leads to two different binding energies of the electron [23, 25].

Figure 3.2 also shows that the energy separation of the doublet decreases with increasing  $l$  for a constant principal quantum number  $n$ . The energy separation of the W 4f peak is only 2 eV, while it is 13 eV of the W 4d peak and 67 eV of the W 4p peak. Furthermore, the spectrum reveals that the peak components have different intensities. The intensity ratio is determined by the number of degenerated substates for a given  $j$  state [12].

A peak, which is always present at very low binding energies (in figure 3.2 at about 5-10 eV), originates from the valence band. Its different states can be better resolved employing ultraviolet light.

For metal samples, additional peaks from the plasmon loss mechanism occur. Photoelectrons penetrating through the solid may excite collective oscillations of the conduction electrons (plasmons). The energy loss depends on the plasmon frequency. Hence, the plasmon peak occurs in a certain distance from the original peak, on its high binding energy side.

Peaks from Auger electrons can also appear in an XPS spectrum. Auger electrons emerge after the photoelectron has left the sample. The remaining core hole is filled by an electron from a higher energy level. The released energy can be emitted as a photon or be transferred to another electron (the Auger electron), which is also

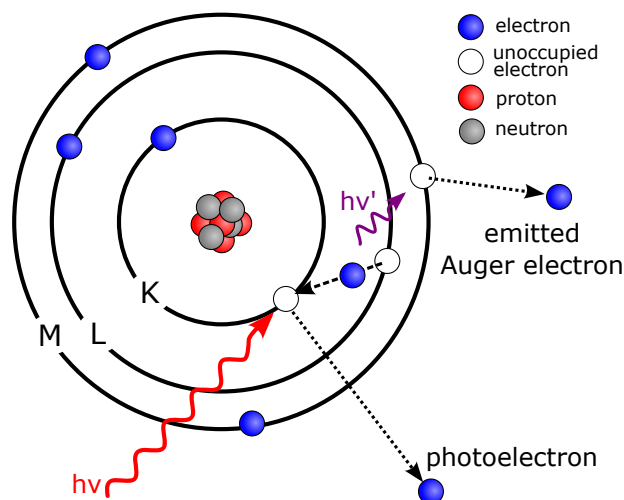


Figure 3.3: Illustration of the photoelectric and the Auger effect. Figure adapted from [26].

ejected from the atom (see figure 3.3). This implies, that the kinetic energy of the Auger electron is independent of the incident photon energy. Hence, Auger peaks can be distinguished from the photoelectron peaks by changing the excitation energy of the photon. The Auger peaks will be shifted in the XPS spectrum whereas the photoelectron peaks stay. The Auger effect is used in an other surface analysis method, namely in the Auger electron spectroscopy (AES) [23, 25].

The photoelectron peaks have a natural broadening which can be calculated from Heisenberg's uncertainty principle:

$$\Delta E = \frac{h}{t}, \quad (3.5)$$

where  $\Delta E$  is the peak width,  $h$  is the Planck constant and  $t$  is the core hole lifetime. The resulting line shape is Lorentzian [23]. Ambient conditions as well as instrumental effects also change the peak shape and determine the peak width. The resolution of the analyzer will cause a Gaussian line shape [25].

Chemical interactions between different elements change the valence electron configuration. This affects the binding energies of the inner electrons, leading to peak shifts in the spectrum. If an elemental component with different binding states is present in a sample, the individual peaks will overlap. This causes an inhomogeneously broadened peak [23]. To separate the different peak components, an elaborate peak-fitting procedure has to be used. The extracted peak parameters are useful for chemical state analysis of the surface .

## Background Subtraction

The determination of the peak intensity is essential for quantitative analysis in XPS. For this reason, different background subtraction methods were developed to separate the actual signal from the background intensity. The easiest way to

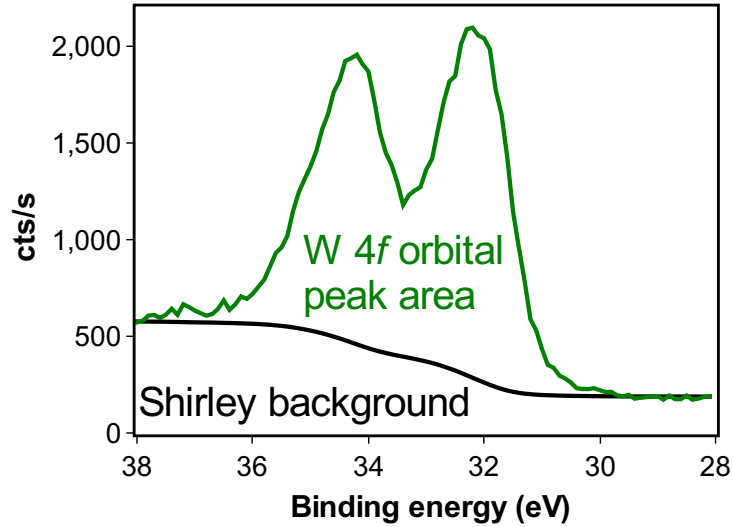


Figure 3.4: High resolution spectrum of the W 4*f* peak (green line). Its Shirley background is calculated according to equation (3.6) and is depicted in the spectrum as black line.

determine the background intensity at the peak location is, to fit a straight line through the continuum intensities on the low and high binding energy sides of the peak. This is a reasonable approximation for insulators [25].

The Shirley background is an other commonly used background. It accounts for the effect of inelastic scattering of electrons [27]. Hence, the background intensity  $B^S(E)$  is considered to be proportional to the integrated intensity  $J(E)$  of the peak, with the lower integration limit  $E_{\min}$  on the low binding energy side of the peak. On the high binding energy side, at  $E_{\max}$ , the background has to match the measured spectrum, thus the normalization factor  $k$  is introduced. The Shirley background can be determined iteratively and is given by

$$B_n^S(E) = k \int_{E_{\min}}^E (J(E') - B_{n-1}^S(E')) dE'. \quad (3.6)$$

$B_0^S(E')$  is the initial guess for the background, which is usually taken to be constant, and  $n$  indicates the iteration step. The Shirley background converges after four to five iterations. This calculation method can be found in commercial XPS data processing systems [25].

The W 4*f* peak of a tungsten sample is shown with its corresponding Shirley background in figure 3.4. In practice, the start and end points for the background are chosen individually for each peak [12]. This makes the background calculation and therefore the peak area to be sensitive to the end points. If the spectrum is very noisy, the signal height around the start and end points should be averaged. Otherwise, the noise will dominate the precision of the peak area calculation [25].

Since the Shirley background method is very sensitive to the integration limits, it is more accurate to use the Tougaard background for the quantitative analysis of the XPS spectra [25]. This background can also be described by equation (3.6), but the constant  $k$  is replaced by the universal cross section  $K(E - E')$  for inelastic electron scattering:

$$K(E - E') = \frac{B(E - E')}{(C + (E - E')^2)^2}. \quad (3.7)$$

This cross section depends on the energy loss and has two coefficients,  $B$  and  $C$ , which depend on the evaluated material. The disadvantage of the Tougaard background is, that for its calculation, the spectrum at the lower binding energy side of the peak has to be known [25]. This means in practice that a survey spectrum has to be acquired.

### 3.3 Analysis Methods with XPS

As stated before, photoelectrons lose energy by inelastic collisions on their way out of the sample. The average length between two inelastic collisions,  $\lambda_i(E)$ , is called the inelastic mean free path. In homogeneous materials, it only depends on the energy  $E$  of the electron [23]. The attenuation of electrons due to inelastic scattering follows the Beer-Lambert law:

$$I(z) = I_0 e^{-\frac{z}{\lambda_i(E) \cos \theta}}. \quad (3.8)$$

$I(z)$  is the intensity of electrons emerging from the depth  $z$ . The attenuation also depends on  $\theta$ , the emission angle of the electrons with respect to the surface and on  $I_0$ , the intensity of photoelectrons originating from the surface [25].  $3 \lambda_i \cos \theta$  is the distance where the intensity drops to 5% of its original value. It is called sampling depth and is about 3-4 nm or the first ten surface layers. Hence, XPS is considered a very surface sensitive method [23].

#### Quantitative Analysis

For a quantitative analysis of an XPS spectrum, the peak area  $I_A$  has to be determined. It is proportional to the abundance of the corresponding element  $A$  in the upper sample layers and depends on several factors [12, 23].

$$I_A = \Gamma_{\text{phot}} T_A(E) L_A(\gamma) \sigma_A(E) t \int_0^\infty n_A(z) \exp\left(-\int_0^z \frac{1}{\lambda_{i,A}(E, n_A(z')) \cos \theta} dz'\right) dz, \quad (3.9)$$

with

- $\Gamma_{\text{phot}}$ , the incident X-ray flux,
- $T_A(E)$ , the transmission function of the analyzer; it depends on the kinetic energy of the incoming electrons,

- $L_A(\gamma)$ , a factor that accounts for the angular asymmetry of the studied orbital, where  $\gamma$  is the angle between the incident photon direction and the emitted electron,
- $\sigma_A(E)$ , the photoionization cross section, which is the probability that an incident X-ray will create a photoelectron from the studied orbital,
- $t$ , the acquisition time,
- $n_A(z)$ , the number density of the studied element at the depth  $z$ ,
- $\lambda_{i,A}(E, n_A(z))$ , the inelastic mean free path of electrons originating from element  $A$ ; it also depends on the particle density of element  $A$ , and
- $\theta$ , the take-off angle of the photoelectrons.

When the elemental composition is homogeneous within the sample (i.e.  $n_A(z) = \text{const.}$ ), then  $\lambda_{i,A}(E, n_A(z))$  is independent of  $n_A(z)$ . This simplifies the integrals and  $n_A$  can be calculated:

$$n_A = \frac{I_A}{\Gamma_{\text{phot}} T_A(E) L_A(\gamma) \sigma_A(E) t \lambda_{i,A}(E) \cos \theta} = \frac{I_A}{I_A^\infty}. \quad (3.10)$$

The quantities in the denominator can be calculated (e.g.  $\sigma_A(E)$ ), measured (like  $I_A$ ), or eliminated by considering only atomic ratios  $n_A/n_B$  (e.g.  $\Gamma_{\text{phot}}$ ) [23].  $I_A^\infty$  combines all these quantities and is referred to as the sensitivity factor [28]. If  $n_A(z)$  is not constant within the sample, its depth distribution can be determined by depth profiling experiments [23].

## Sputter Depth Profiling

To obtain a sputter depth profile, energetic ions (0.5-5 keV) bombard the sample and gradually remove its surface [25]. Alternately, XPS spectra are acquired which analyze the remaining surface. To avoid surface contamination by redeposition of the residual gas, the acquisition time between two sputter steps should be as short as possible [23]. To still get a good signal-to-noise ratio, short range spectra around the peaks are acquired.

Noble gases are used as projectile material since they do not undergo chemical reactions with the target. The ion beam has to be highly pure, otherwise reactive impurities, which remained in the beam, will be implanted into the investigated sample during the sputter process. Besides, the ion beam is optimized by means of a Faraday-cup in such a way, that the maximum sample current and the minimum beam spot size is reached [25].

High ion energy and low incident angle increase not only the sputter yield but also the specimen damage. This ion-beam-induced damage leads to a mixing of the different components and can change the concentration ratios in the uppermost layers [25].

As stated before, different materials have different sputter yields. This can lead to a non-uniform removal of material from inhomogeneous samples and makes the conversion of depth profiling data into an actual depth scale only possible, if depth profiling calibration has been performed [25]. In the scope of this work, it was not attempted to convert the depth profile of the WN system into an absolute depth scale, but the experimental data were compared to the N depth distribution obtained from simulations (see section 4.3).

### 3.4 Instrumentation

Commercial stand-alone instruments for XPS analysis are available since the seventies of the last century. The main component is an ultra-high vacuum (UHV) chamber with an X-ray source and an analyzer-detector system. Additional instruments, like the ion sources, are added to the UHV system for in-situ manipulation of the sample. Components used at the XPS device for this work, a PHI ESCA 5600 (see figure 3.5a) are explained in the following paragraphs.

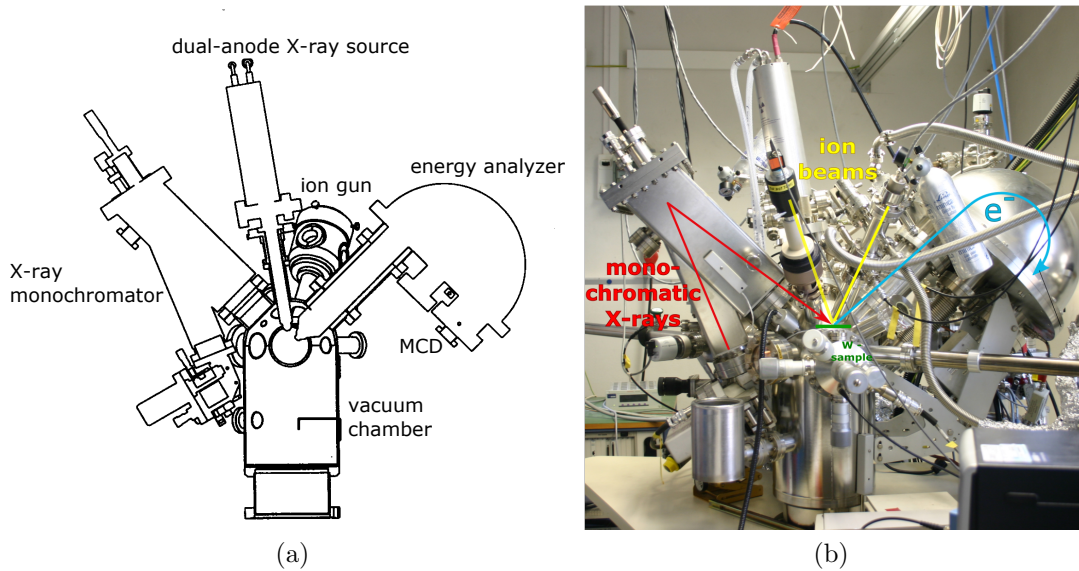


Figure 3.5: A schematic diagram (a) and a picture (b) of the PHI Model 5600 MultiTechnique system with the most important components. Schematic from [29].

#### UHV Technology

Ultra-high vacuum conditions are required for XPS analysis. The emitted photoelectrons must not lose kinetic energy due to collisions with surrounding gas particles on the way to the analyzer. The mean free path of the electrons is inversely proportional to the gas pressure  $p$  and it is  $10 \cdot 10^5$  cm for  $p = 10^{-3} - 10^{-7}$  mbar [30]. This constrains to high vacuum conditions in the vacuum chamber.

Furthermore, the surface composition of the object of study must not change during acquisition. The time  $\tau$ , which is needed to cover the sample surface by a monolayer of gas particles, depends on the particle density  $n$  of the surrounding gas, the average velocity  $\bar{c}$  of the gas particles and on  $a$ , the number of sites on the surface which can be occupied by the gas particles per unit area:

$$\tau = \frac{4a}{n\bar{c}}. \quad (3.11)$$

This time scale is  $\geq 100$  s for an ambient gas pressure of  $10^{-9}$ - $10^{-10}$  mbar [30]. Since the acquisition time for the XPS spectrum is at least 100 s, ultra-high vacuum ( $10^{-7}$ - $10^{-12}$  mbar) conditions are needed in the vacuum chamber [23].

The main vacuum enclosure is made from non-magnetic stainless steel. A load lock is linked to it, to transfer the sample from ambient to UHV conditions without breaking the main vacuum. To maintain a pressure of about  $10^{-10}$  mbar in the main chamber, different pumping systems are used and the vacuum chamber is baked out at approximately 500 K for several hours before operation. Condensed particles, especially water, will degas from the walls and can be pumped out of the system [25].

## The X-ray Source

The X-ray production is based on a conventional X-ray tube. Electrons emitted from hot filaments are accelerated to about 15 keV and impinge on the anode. There, they produce a typical X-ray spectrum with a background (Bremsstrahlung) and the characteristic emission lines, produced by fluorescence of the anode material. The characteristic lines of the material are used in XPS experiments since their intensity is orders of magnitude higher than that of the Bremsstrahlung [25]. The common anode materials are aluminum (Al) and magnesium (Mg). In both cases, the  $K_\alpha$ -line<sup>8</sup> is used [23, 25]. Their energies and their line widths are listed in table 3.1.

Emission line	Energy (eV)	Width (eV)
Al $K_\alpha$	1486.6	0.85
Mg $K_\alpha$	1253.6	0.7

Table 3.1: Characteristic energies and line widths for XPS anode materials.

Many XPS sources use a dual anode where the anode itself is made from copper and the wedge-shaped faces are coated with Al and Mg [25]. To improve the energy resolution of XPS a monochromator is used. The Al anode, which emits light at a wavelength of  $\lambda = 0.83$  nm ( $K_\alpha$ -line), is combined with a quartz crystal, which has a lattice spacing  $d = 0.425$  nm. For this system, the Bragg relation

$$n\lambda = 2d \sin \theta, \quad n \in \mathbb{N} \quad (3.12)$$

<sup>8</sup>This is the transition of an electron from the orbital with quantum number 2 to the innermost orbital, referred to as K-shell, with quantum number 1.

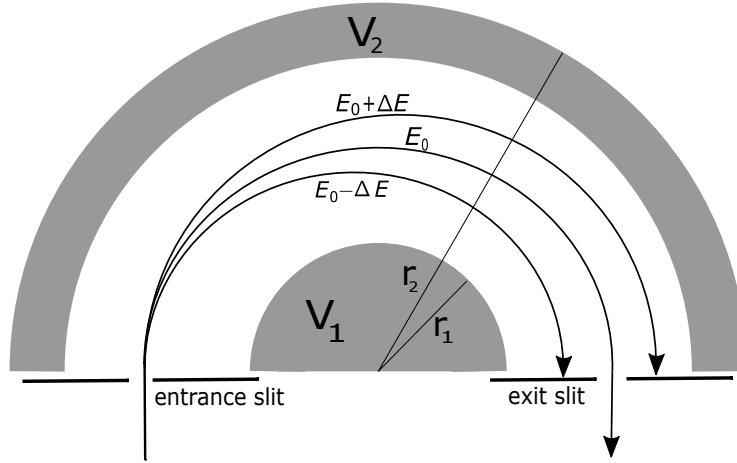


Figure 3.6: The energy selection principle of the electrostatic hemispherical analyzer.

is fulfilled at an angle  $\theta$  of  $78^\circ$  and the X-rays of wavelength  $\lambda$  interfere constructively. The monochromator also prevents weaker X-ray fluorescence lines striking the sample. Otherwise, they appear as undesired satellite peaks in the XPS spectrum. The disadvantage of the monochromator is, that it also reduces the intensity of the X-ray light [23, 25].

## The Analyzer - Detector System

The analyzer of the PHI ESCA 5600 is an electrostatic hemispherical analyzer (HSA). It consists of two concentric hemispheres with radius  $r_1$  and  $r_2$ . A constant potential

$$V_2 - V_1 = V_0 \left( \frac{r_2}{r_1} - \frac{r_1}{r_2} \right)$$

is maintained between the two hemispheres, with  $V_0$  being the potential on the center line. Only electrons which enter the HSA with an energy of

$$E_0 = eV_0 \quad (3.13)$$

can pass the slit on the exit plane (see figure 3.6).  $E_0$  is therefore called the pass energy. Electrons with slightly different energies or entering under an angle  $\alpha_{\max}$  around the central ray will not be focused on the exit slit but still reach the output plane [31]. If the analyzer is run in the fixed analyzer transmission (FAT) mode, the pass energy is kept constant over the whole acquisition range, which reaches from 0 eV up to 1500 eV.

An electric lens system in front of the analyzer collects the photoelectrons and focuses them onto the entrance slit. It also retards the electrons to the pass energy of the analyzer by applying an electrostatic field. The higher the collection angle of the lens, the higher is the number of photoelectrons collected per incident X-ray. However, the energy resolution is reduced. To avoid this, an aperture is placed in front of the analyzer [23, 25]. The efficiency of the lens system is not constant over

the complete acquisition range and depends on the pass energy  $E_0$ . This energy dependence is included in the transmission function of the analyzer, an intensity scale which has to be taken into account for a quantitative analysis of the XPS spectra [25].

The FAT mode is generally used for XPS measurements, since the energy resolution of the analyzer is constant over the whole acquisition range (see equation (3.14)) [25]. Due to the finite slit width  $w$  and the acceptance of electrons entering under an angle  $\pm\alpha_{\max}$ , the narrowest line width ( $\Delta E$ ) that can be measured by the analyzer is [32]:

$$\Delta E = E_0 \left( \frac{w}{r_1 + r_2} + \frac{\alpha_{\max}^2}{4} \right). \quad (3.14)$$

From this equation it can be seen that lower pass energy means better resolution. The acquisition time for a high resolution spectrum, however, has to be increased to reduce statistical errors.

For detection, a multichannel detector is used. The advantage compared to the simple exit slit is its improved energy resolution. The initial energy of the electrons can be extracted from their detection position. The channels themselves count the number of electrons entering. Therefore, each channel is constructed as an electron multiplier. Its cylinder is made from semiconducting material, where a potential difference is applied along the wall. An electron hits the wall and produces secondary electrons which are also accelerated. They collide several times with the wall, thus producing a cascade of electrons, which is, in the linear regime, proportional to the original number of electrons [25, 31].

## The Ion Source

An ion source is not mandatory to perform XPS measurements but it is a useful tool for surface cleaning and in situ manipulation of the sample. In the scope of this work, it was employed for ion implantation and sputter depth profiling. Many different types of ion sources exist. For XPS, the electron impact type is usually applied [25].

Electrons are emitted from a heated filament and accelerated to the anode, a grid cylinder. There, they collide with the neutral gas molecules. The electrons ionize the atoms and produce an electron-ion plasma. The ions get extracted from the plasma by applying the voltage  $U_{\text{ext}}$  and form an ion beam. The beam is focused via electric lenses and can be adjusted to hit the sample via deflection plates [33].

To get a well defined ion beam, a Wien mass filter can be mounted to the ion source. It consists of a magnet and a pair of electrostatic plates which produce an electric field  $\mathbf{E}$  perpendicular to the magnetic field  $\mathbf{B}$ . The ions are accelerated to

$$E_{\text{kin}} = \frac{1}{2}mv^2 = QU_{\text{ext}}, \quad (3.15)$$

with  $Q$ , the electric charge. Assuming, that the acceleration is perpendicular to both the  $\mathbf{E}$  and the  $\mathbf{B}$  field, the ions can pass the Wien filter if their velocity satisfies

$$v = \frac{|\mathbf{E}|}{|\mathbf{B}|}. \quad (3.16)$$

From equation (3.15) it can be seen that the velocity depends on both the mass and the electric charge of the particle. By adjusting  $\mathbf{E}$  and  $\mathbf{B}$ , impurities and different ionization states can be separated from the beam [34].

# Chapter 4

## Experimental Procedure

If not stated differently, the work as it is described in this chapter and the presented experiments, as well as their evaluation were done by me.

The tungsten samples used for the experiment are hot rolled tungsten plates produced by PLANSEE with a purity of 99.97 mass percent [4]. They are 12 mm  $\times$  15 mm in size with a thickness of 1 mm. To guarantee a smooth and clean surface, the tungsten plates undergo the following cleaning procedure: First they are ground and then polished [35]. The remaining polishing paste is removed from the sample by applying an ultra sonic bath in acetone. Afterward, impurities from the bulk and internal mechanical stress are removed, by annealing the sample under vacuum conditions at 1200 K for two hours in a molybdenum oven. Samples which are not used immediately are stored in a desiccator.

Sample analysis is performed in a commercial XPS device, a PHI ESCA 5600. The base pressure in the main vacuum chamber ranges from  $9 \times 10^{-11}$  mbar to  $1.5 \times 10^{-10}$  mbar. The sample can be heated up to 900 K in the specimen holder. Nitrogen is implanted in situ into the tungsten sample via a Wien filtered SPECS IQE 12/38 ion source, which is mounted at an angle of  $45^\circ$  to the sample surface [4]. The Wien mass filter is used to get a pure  $N_2^+$  ion beam.

The ion source was operated at an acceleration voltage of 600 V. Lower voltages are not accessible since internal ion interactions become dominant. These would make the beam unstable. The energy per nitrogen atom is then 300 eV. This is close to the upper limit of the ion impact energy  $E_i$  with which the nitrogen ions from the edge plasma collide with the reactor wall.

The energy of the plasma ions impinging on a surface can be calculated via [36]:

$$E_i \approx 2T_i + 3ZT_e, \quad (4.1)$$

where  $T_i$  is the ion and  $T_e$  the electron temperature, respectively.  $Z$  is the charge number of the ion. For a temperature between 1 and 30 eV, as it occurs at the divertor target, the charge number of nitrogen ranges from one to five. This, inserted into equation (4.1) under the assumption that  $T_i \approx T_e = T$ , gives an energy range of 5-500 eV for the nitrogen ions.

Another SPECS IQE 12/38 ion source without Wien mass filter is employed to clean the sample surface from carbon and oxygen adsorbates and surface oxides. It is

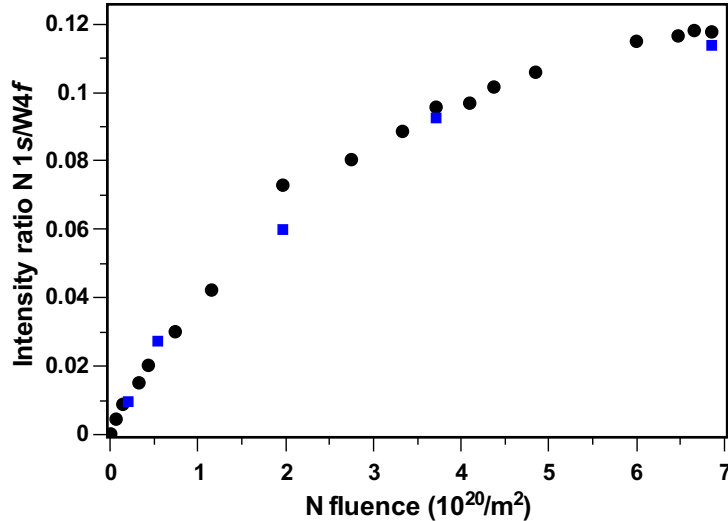


Figure 4.1: Comparison of the two applied X-ray sources. For the N fluence series at 300 K, once the dual-anode source (blue squares) and once the X-ray source with the monochromator (black circles) was used. The measured intensity ratios are the same for both X-ray sources.

also used for sputter depth profiling. Ar ions of 1 keV energy hit the sample surface at an angle of  $40^\circ$  [4]. Under these conditions, an argon fluence of  $1 \times 10^{20} \text{ m}^{-2}$  sputters approximately 2 nm of pure tungsten.

Alternating to the ion bombardment (N implantation and Ar sputtering), XPS spectra are acquired. In most cases, the sample was irradiated by a monochromatic X-ray source which delivers X-ray photons with an energy of 1486.7 eV and a line width of 0.5 eV [37]. Due to technical problems, the monochromatic X-ray source could not be used for all measurements. The Al  $K_\alpha$ -line of the dual-anode source was used instead. A comparison of an N implantation fluence series at 300 K employing once the monochromatic (black circles) and once the dual-anode source (blue squares) shows no difference in the measured intensity ratios (see figure 4.1).

Emerging photoelectrons produced by X-ray irradiation enter the analyzer via an OmniFocus III lens system. The analyzer is positioned in  $45^\circ$  to the normal vector of the sample surface and in  $90^\circ$  to the monochromatic X-ray source. The angle between the analyzer and the dual-anode X-ray source is  $54.7^\circ$  [29]. The analyzer is operated in the FAT mode and a pass energy of 93.9 eV is chosen for the survey and the fluence series. For high resolution measurements, a pass energy of 11.75 eV is chosen with an additional reduction of the lens system's aperture.

## 4.1 Preparation of the XPS Device

Before the start of this experiment series, the vacuum system was vented to repair the thermocouple at the specimen holder and to exchange a pressure gauge at the

Wien-filtered ion source [17]. After venting the vacuum system, it was baked out and the different components which were used for the measurements were prepared for the operation restart. The filaments of both X-ray sources were outgassed as well as their anodes. The anodes and the HV-isolators were then conditioned by a stepwise increase of the high voltage. Additionally, the monochromator had to be aligned. To this end, a silver (Ag) sample was mounted in the main chamber. The Ag  $3d_{5/2}$  peak at 368 eV is very narrow and intense and its width is determined by the width of the the X-ray light. The monochromator is aligned, when the signal intensity of the Ag peak is maximal and the peak width is narrowest.

A microscope and camera system is mounted to the XPS device to position the sample for the experiment. For its alignment, a Ag sample with slits of different sizes and a small hole in the middle was transferred to the specimen holder. The specimen holder was moved until a minimum in the XPS signal indicated that the slit was found. Then, the microscope was focused to this slit and the aperture size of the analyzer was reduced. The procedure was repeated until the small hole of the Ag sample was in focus of the microscope.

As a next step, the ion source was degassed to guarantee a clean ion beam. Afterward, the beam was aligned and focused on the sample by adjusting the voltages of the electric lens system (see also section 4.5). Therefore, a Faraday-cup was transferred into the vacuum chamber and the current on the sample and on the Faraday cup was measured. Optimal focus and alignment of the beam is reached when the ratio of the current in the Faraday cup to the sample current is maximal. At the Wien-filtered ion source, the permanent magnet was mounted additionally and the electric field of the Wien filter was adjusted.

In the last step, the hemispherical analyzer was conditioned. First, the voltage of the MCD was adjusted. For this purpose, the Ag sample was mounted again and test measurements were acquired once using the monochromatic and once the dual-anode X-ray source. The best count rate was achieved at a multiplier voltage of 2200 V. Then, the HSA was calibrated. Besides the Ag sample, gold (Au) and copper (Cu) samples are used for calibration. Their peaks appear in different energy ranges of the spectrum (Au  $4f_{7/2}$  at 84 eV and Cu  $2p_{3/2}$  at 933 eV). From the acquired spectra, the work function of the detector was calculated to be 4.2 eV.

## 4.2 Evaluation of XPS Spectra

To determine the N concentration in the W surfaces from the XPS spectra, the Shirley background is calculated and subtracted from the N  $1s$  and W  $4f$  peaks. This is done with the data processing program MultiPak version 9.0. The integration limits are set manually to 393 eV and 405 eV for the N  $1s$  peak. For the W  $4f$  peak, they are set to 26 eV and 44 eV. Once the peak areas are calculated, they are divided to obtain the intensity ratio. For a comparison with experimental data from [10] and with simulations (see section 4.3), the ratios are corrected for the Tougaard background. As suggested in [4], for a WN system this can be approximated by multiplying the intensity ratio with a factor of 1.42.

A number of error sources have to be considered in the quantitative analysis of the XPS spectra. Systematic errors emerge, for instance, due to the dependence of the analyzer's transmission function on the sample position. An other source of systematic errors cannot be excluded: A defect electronic board of the analyzer's lens system, which could only be identified at the end of this work, caused a step in the acquired XPS spectra which emerged only occasionally. Its occurrence can influence the ratio of the peak intensities and therefore the quantitative analysis. As soon as it was visible in the spectrum, the measurement was stopped. Since short range spectra were acquired for most of the measurement series, the step could have also occurred outside of the detection range. For most of the measurements its occurrence can not be excluded. The defect electronic board was replaced before the depth profile at 800 K (see section 5.3) was acquired.

Two unavoidable uncertainties come with the duration of the measurement. First, with increasing ion fluence (see section 4.4), the sample roughness increases. The changes in morphology are, however, small and therefore negligible [10]. Second, adsorption of residual gas in the vacuum chamber onto the sample surface occurs during data acquisition. The layer of adsorbed gas molecules will grow with acquisition time and absorb parts of the passing electrons. An experiment was performed to quantify this uncertainty.

Figure 4.2 shows the N 1s to W 4f intensity ratios after an implantation of N in W at 300 K. The first data point was acquired directly after the ion implantation. Then, the sample stayed at 300 K for 13 h without ion bombardment. During this time, residual gas, including nitrogen, could adsorb onto the sample surface. The second data point was acquired after the resting time. Subsequently, the sample was irradiated with N ions for 1.5 h. Since the N content in the sample was already in saturation after the first implantation, the nitrogen content remained the same during the second ion bombardment, but the surface was cleaned by sputtering the adsorbed material. After ion irradiation, the last data point was acquired. The statistical error of the measurement is significantly lower than the scatter of the data. This shows, that the scatter due to surface contamination accounts for ca. 5 % of the intensity ratio. However, it cannot be excluded from this measurement that other parts of the measurement technology also account for the scatter in the data. The error due to surface contamination should be negligible for all acquired fluence series and sputter depth profiles, since the surface is cleaned by the bombarding ion.

For this reason, only statistical errors originating from the detection process are calculated for these measurements. The detection of single electrons follows a Poisson distribution which converges for a large number of counts ( $N$ ) to a Gaussian distribution. The standard deviation ( $\sigma$ ) of the detected signal is then equal to  $\sqrt{N}$ , which is the statistical error of the detected counts. Since the signal-to-noise ratio of the W 4f is very high, its statistical error is negligible and the following procedure is only performed for the N 1s peak. As the first step, the number of detected electrons per channel is determined. Then, the measured count rate is multiplied by the acquisition time in a routine written by G. Meisl and me.

This modified spectrum serves as input for the program which calculates the Shirley background according to equation (3.6) and the statistical error of the peak

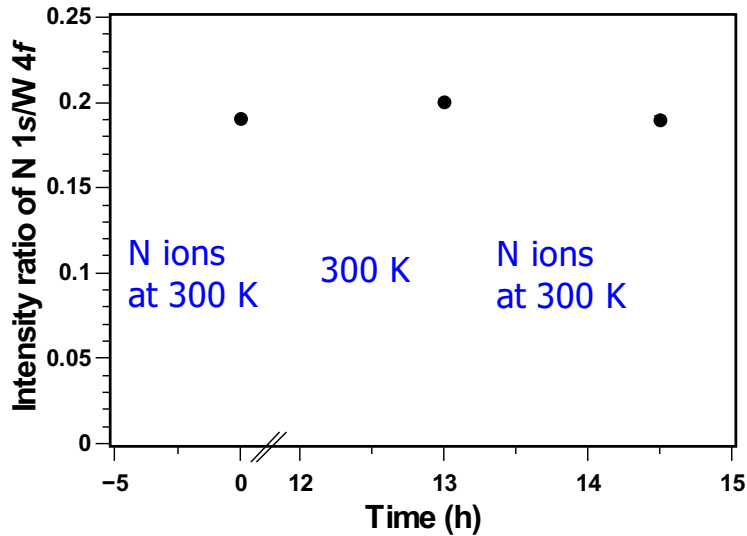


Figure 4.2: Scatter of the XPS measurements due to surface contamination. A sample was implanted with N ions of 300 eV at 300 K until saturation (first data point). It stayed for several hours under UHV conditions unattached at 300 K (second data point) until it was bombarded with N ions again (third data point). The pass energy of the analyzer was 11.75 eV for the three data points. The statistical error is included in the symbol size.

area [38]. As stated before, the Shirley background is sensitive to the level of the start and end points. For this reason, the acquired peak spectrum is manually split into three regions. The first region consists only of background. It ranges from 393 eV to 395 eV for the nitrogen peak. The signal in this region is averaged over the channels and the standard deviation is calculated as the square root of the averaged signal [38].

In the second region (395 eV to 402 eV for the N 1s peak), both the background signal ( $N_B$ ) and the signal  $N_{el}$  originating from the photoelectrons are present. If  $N_S$  is the total number of detected counts in a single channel, then

$$N_{el} = N_S - N_B. \quad (4.2)$$

The error of  $N_{el}$ ,  $\sigma_{el}$ , can be calculated via propagation of uncertainty [38]. It is

$$\sigma_{el} = \sqrt{\sigma_S^2 + \sigma_B^2} = \sqrt{N_S + N_B}, \quad (4.3)$$

with  $\sigma_S$  and  $\sigma_B$  being the standard deviation of  $N_S$  and  $N_B$ , respectively.

In the third region (402 eV to 405 eV for the N 1s peak), only the Shirley background, with a level higher than in the first region (see section 3.2), is present. Its signal is again averaged over the channels and  $\sigma_{el}$  is calculated as the square root of the averaged counts. To get the absolute statistical error of the complete photoelectron peak, the standard deviations  $\sigma_{el}$  of the channels or regions are summed up [38].

### 4.3 Forward Calculation

To obtain the N concentration in the surface from the evaluated XPS spectra, either sensitivity factors have to be used or the spectra need to be compared to simulations. A direct comparison between the peak intensity ratios and the depth distribution of SDTrimSP simulations is not possible. As mentioned in section 3.3, the XPS method has a sampling depth of  $3\lambda_i \cos\theta$ . The XPS signal is, according to the Beer-Lambert law, an exponentially weighted average over this depth with the largest contribution from the surface. The extraction of the actual depth distribution from this signal is difficult. An easier approach is to transform a given depth profile into XPS intensity ratios by applying equation (3.9) [4]. They can be compared to the experimental data. For their calculation, a given depth profile has to be split into layers of homogeneous composition.

SDTrimSP depth profiles are already given in layers of thickness  $\Delta x_k$  and a homogeneous particle density  $n_{A,k}$ . The intensity  $I_{A,k}$  of layer  $k$  and element  $A$  employing equation (3.8) is:

$$I_{A,k} = \xi_A n_{A,k} \lambda_k \left( 1 - \exp\left(\frac{-\Delta x_k}{\lambda_k}\right) \right), \quad (4.4)$$

where  $\xi_A$  contains all prefactors and  $\lambda_k$  is the inelastic mean free path of layer  $k$ . The total intensity is obtained by summing up the intensities from all layers [12]. This results in:

$$I_A = \sum_k I_{A,k} \exp\left(-\sum_{j=0}^{k-1} \frac{-\Delta x_j}{\lambda_j}\right). \quad (4.5)$$

The explained procedure is also illustrated in figure 4.3.

The forward calculation of the SDTrimSP N depth profile (figure 2.2) in section 5.1 was performed by Olaf Encke [10]. The forward calculations in section 5.2 were done by Gerd Meisl [17].

### 4.4 Fluence Calculation

To study the build up of the N content and the depth distribution by sputter depth profiling, the ion fluence  $\Phi$  has to be known. It is the number of incident ions per area and can be determined via

$$\Phi = \frac{1}{Q_i A} \int_0^t I_{\text{sample}}(t') dt'. \quad (4.6)$$

The integration limit  $t$  is the time until the sample is exposed to the ion beam.  $Q_i$  is the electric charge of the ion,  $A$  is the area irradiated by the ion beam and  $I_{\text{sample}}(t)$  is the measured sample current. For a correct determination of the current, the secondary electrons have to be taken into account. They leave the surface when the ion beam hits the sample, thus adding to the electrical current produced by the

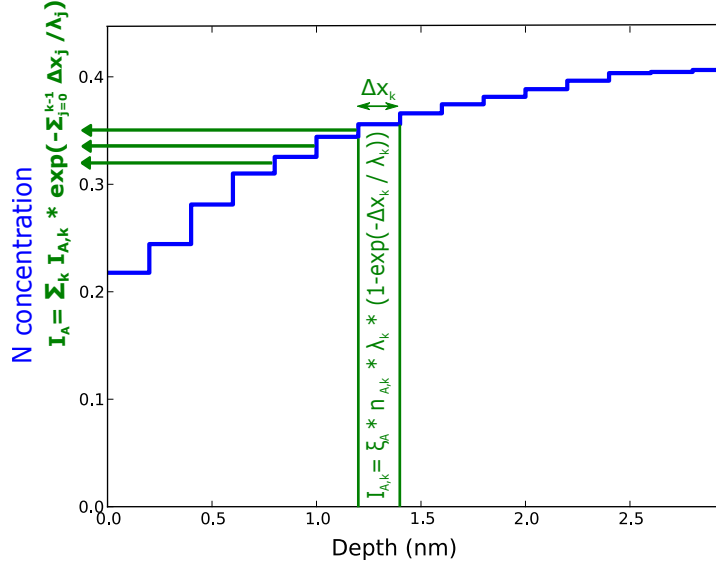


Figure 4.3: Illustration of the forward calculation for a given SDTrimSP N depth profile. Figure adapted from [4].

impinging ions. In earlier experiments, a bias voltage could be applied to the sample which suppresses the secondary electron loss. These experiments show, that for the present implantation conditions, the secondary electrons account for about 10% to the measured current. This amount is subtracted from  $I_{\text{sample}}$ .

It should be mentioned that the fluence calculation contains systematic errors. A careful determination of the irradiated area  $A$  was performed to reduce the uncertainty (see section 4.5). The main contribution to the error comes from the determination of the sample current. A constant sample current over a time scale of several hours is difficult to achieve, since it depends on the gas pressure in the ion source, which is very unstable. The integration of the current over time is hard to perform manually and is replaced by a summation of time intervals with constant  $I_{\text{sample}}$ . However, the systematic errors are not calculated since the measurements are in good agreement with experimental data from [10] and with the simulations (see chapter 5).

## 4.5 Characterization of the Ion Source

The undisturbed ion beam has a Gaussian profile with a full width at half maximum (FWHM) of about 0.8 mm for the Wien filtered and 1.5 mm for the unfiltered ion source. To attain homogeneous ion irradiation on the sample, the N ion beam is rastered over an area of 5 mm  $\times$  5 mm and the Ar beam over 4.5 mm  $\times$  4.5 mm. The actual area is, however, larger, because the widened beam superposes with the scanned area. This is made visible by directing the ion beam on an amorphous hydrocarbon film. The impinging ions remove atomic layers of the film, where the amount of removed material depends on the beam intensity. The interference of visible light reflected by the hydrocarbon film marks the bombarded region. The

exact shape and size of the scanned area is determined by analyzing the sample under an optical microscope.

The first investigations revealed that the nitrogen beam spot at 300 eV ion energy was inhomogeneously widened (see figure 4.4a). The shape could be improved and the size reduced by adjusting the extractor voltage of the ion source as well as the voltages of the focusing electric lens system. The result is shown in figure 4.4b.

The rastered area was generated with a 2.5 keV ion beam, because the beam size is negligible at high energies. At low energies, the interaction between the ions in the beam becomes dominant and leads generally to a widened beam spot. Figure 4.5a shows that before any adjustment, the rastered area was irradiated inhomogeneously. By increasing the time per dot of the raster mechanism, the homogeneity could be increased. Another problem was that the rastered area was neither orthogonal nor equilateral. This is due to the following: The ion source is mounted under the angle  $\theta$  and the deflection plates are tilted under the angle  $\phi$  to the sample surface. These two angles are needed for an internal algorithm to apply appropriate voltages to the deflection plates. An incorrect  $\theta$  will lengthen one axis, while a wrong  $\phi$  will alter the deflection angle. Re-measurement and re-calculation of both angles led to an almost quadratic area as it can be seen in figure 4.5b. A similar procedure was pursued with the unfiltered ion source. In this case, the beam is more stable due to the higher energy of the Ar ions. Furthermore, the ion source is only tilted in  $\theta$  direction with respect to the sample surface. This facilitates the adjustment of the deflection voltages. Finally, the complete rastered area of the nitrogen beam was determined to be 33 mm<sup>2</sup> and 36 mm<sup>2</sup> for the argon beam.

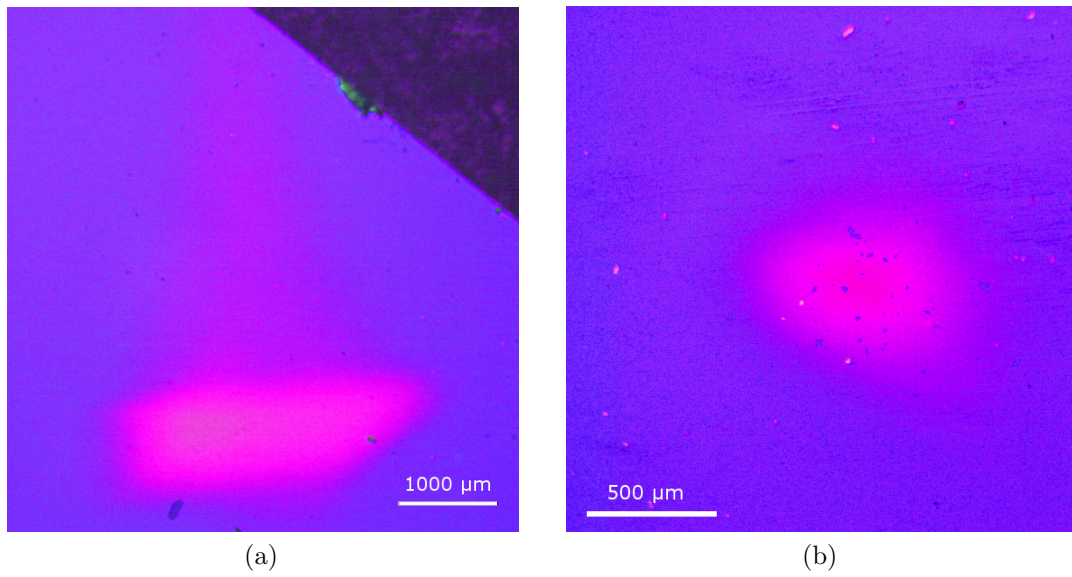


Figure 4.4: (a) Optical microscope picture of a hydrocarbon film irradiated with the Wien filtered nitrogen beam spot at 300 eV ion energy. The spot (magenta) is highly distorted. (b) Improved beam shape and size after the voltage adjustment of the ion source's extracting and focusing elements.

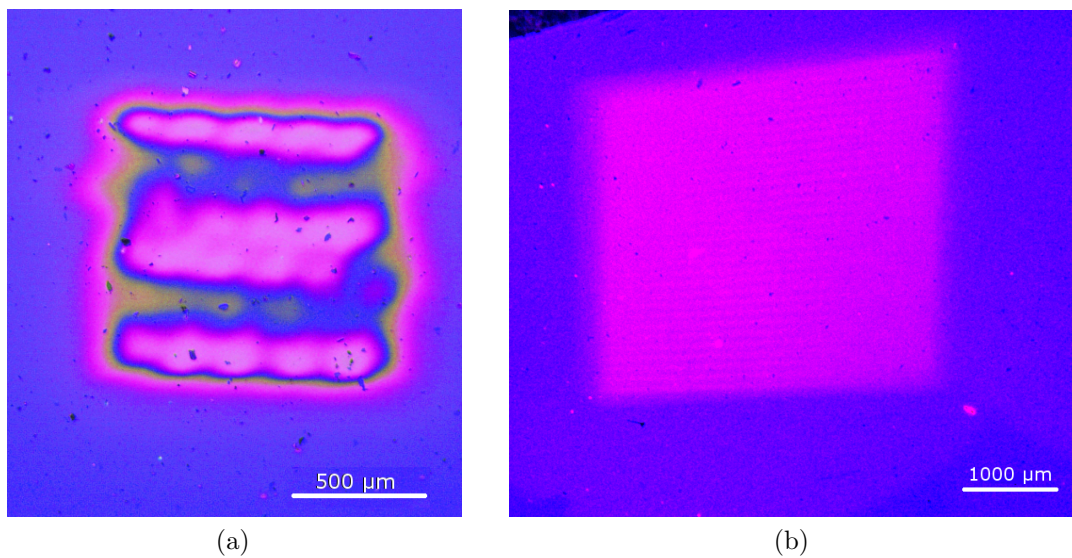


Figure 4.5: (a) Inhomogeneously rastered area of 1 mm  $\times$  1 mm size with a nitrogen beam of 2.5 keV per atom. (b) Rastered area of 4 mm  $\times$  4 mm size after adjustment procedure.

# Chapter 5

## Results and Discussion

Previous experimental results show, that WN layers created by implantation of 2.5 keV N ions into tungsten decompose only above 900 K sample temperature [4]. This observation contradicts thermodynamic calculations which predict a phase change already at 600 K [39]. Further experiments with 2.5 keV ions revealed, that the N content decreases gradually with increasing implantation temperature in the range of 300 K to 800 K [12]. For a more detailed evaluation, further implantation series in this temperature range were performed in the scope of this thesis. A N ion energy of 300 eV was chosen, since the implantation depth is smaller for lower kinetic energies and fits better to the sampling depth of XPS (see section 3.3). Moreover, the ion energy of 300 eV lies in the relevant energy range of N impurities impinging onto the divertor plates of a tokamak (see chapter 4). Sputter depth profiles were also performed for the different implantation series. They should reveal whether the N depth distribution and the N erosion depend on the temperature.

### 5.1 Annealing after Implantation

In the first experiment, the aim was to check the previous results, this means to determine whether the WN phase is stable in the investigated temperature range. On this account, a tungsten sample was implanted with nitrogen at 300 K. The N 1s/W 4f intensity ratio saturated at a fluence of approximately  $6 \times 10^{20} \text{ m}^{-2}$  which corresponded roughly to an implantation time of six hours. Saturation is reached, when the XPS intensity ratio is constant within the uncertainties discussed in section 4.2. After implantation, the sample was heated to 800 K and held at this temperature for 5 h.

The XPS intensity ratios, acquired before and during this time are shown in figure 5.1. They were measured with a pass energy of 11.75 eV. The data points (blue), which were acquired during annealing, scatter around a value of 0.158 (black horizontal line). This observation shows, that the formed tungsten nitride does not decompose between 300 K and 800 K on a time scale of several hours.

The main contribution to the scatter in the data is the re-adsorption of residual gas. This is confirmed by the raw data (not shown), which reveals a carbon and

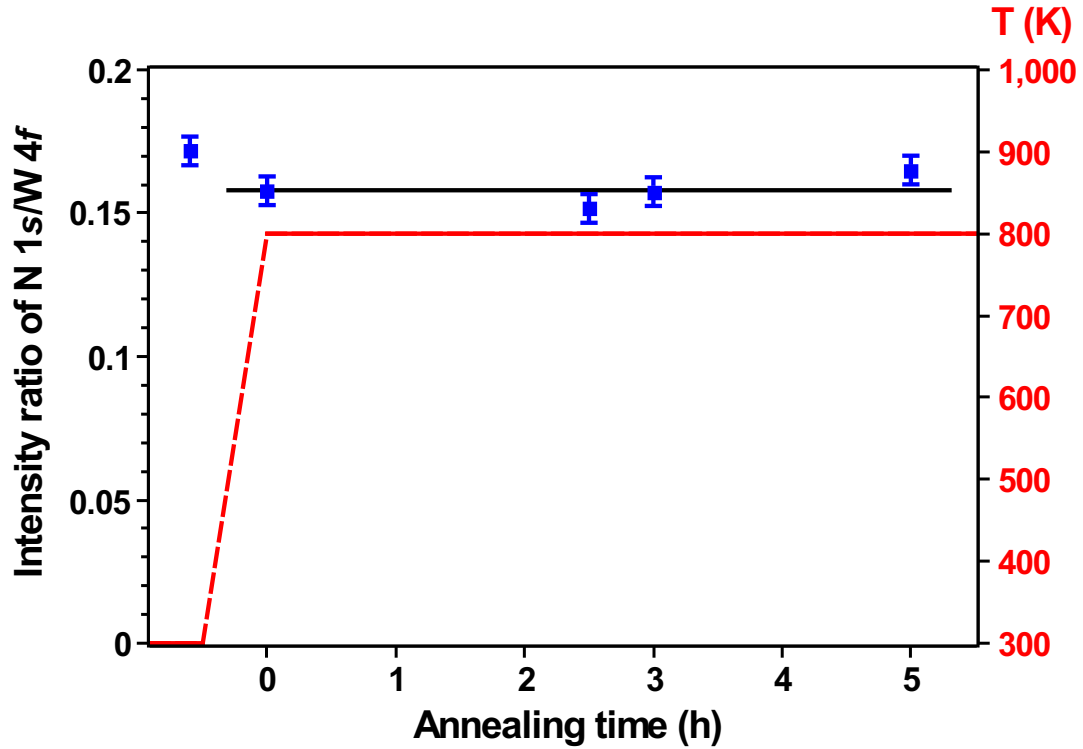


Figure 5.1: XPS intensity ratios (blue squares) for a W sample, implanted with N at 300 K and subsequently heated to 800 K. The red line indicates the temperature profile. The data points scatter around a constant value of 0.158 (black line), thus indicating that the WN phase is stable up to 800 K.

oxygen contaminated surface after several hours of annealing. The error bars indicate the scatter due to this effect as it was observed in the experiment shown in figure 4.2.

To examine whether the N content stays the same after annealing and to investigate its depth distribution, a sputter depth profile was measured. It is shown in figure 5.2 (blue squares) and compared to the reference (black circles), the depth profile of an implantation at 300 K without subsequent annealing. The magenta line shows the calculated Ar sputter depth profile of the SDTrimSP simulation (cf. figure 2.2). All curves agree within the uncertainties of the measurements, confirming that the N content is not changed by the annealing process.

The depth profiles were measured at 300 K. Since these measurements were acquired with a pass energy of 93.9 eV, they cannot be directly compared to the values of the intensity ratios shown in figure 5.1. The two measured depth profiles show the same behavior excluding the two first data points. A possible explanation is, again, that residual gas has been re-adsorbed on the surface of the annealed sample during the annealing time. In contrast, the Ar depth profile of the reference was performed immediately after the implantation.

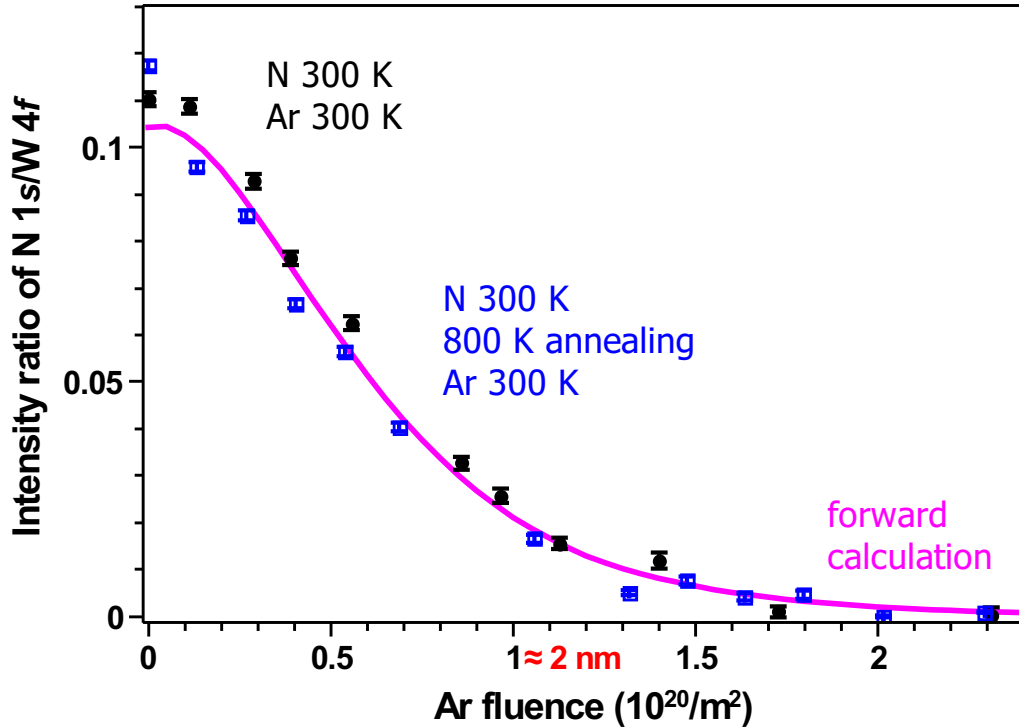


Figure 5.2: Depth profiles at 300 K of samples where nitrogen was implanted at 300 K. One sample (blue squares) was heated up to 800 K after implantation, the other not (black circles). The error bars indicate the statistical error. Both profiles show the same behavior, which implies that the WN phase is stable on a time scale of a few hours. The profiles are also in good agreement with the simulated XPS signal (magenta line) for the N distribution shown in figure 2.2 [10].

The measured curves have the same shape. This shows, that the underlying N distribution is the same in both cases. The good agreement of the data also implies that the erosion properties of the formed tungsten nitride is not influenced by annealing the sample to 800 K. The area under both curves is approximately the same. This means that the N content in the surface stays constant for both the annealed sample and the sample without annealing. From these observations, it can be concluded that the WN phase is stable on the time scale of several hours.

As discussed in [10], the measured curves are also in good agreement with the XPS depth profile from forward calculations (magenta line). It was calculated for a nitrogen distribution obtained by an SDTrimSP simulation with 300 eV N ions (see figure 2.2). This implies that nitrogen implantation in tungsten can be simulated employing the binary collision approximation.

## 5.2 Implantation at Different Temperatures

To see whether the WN formation is influenced by the temperature, N was implanted into W at different temperatures, ranging from 300 K to 800 K. The data is shown in figure 5.3. It can be seen, that the N saturation level is gradually reduced with increasing temperature. This observation contradicts the predicted occurrence of a phase change at 600 K. The statistical error of the data was calculated as described in section 4.2. This is smaller than the symbol size representing the measured data. The except is the fluence series at 800 K.

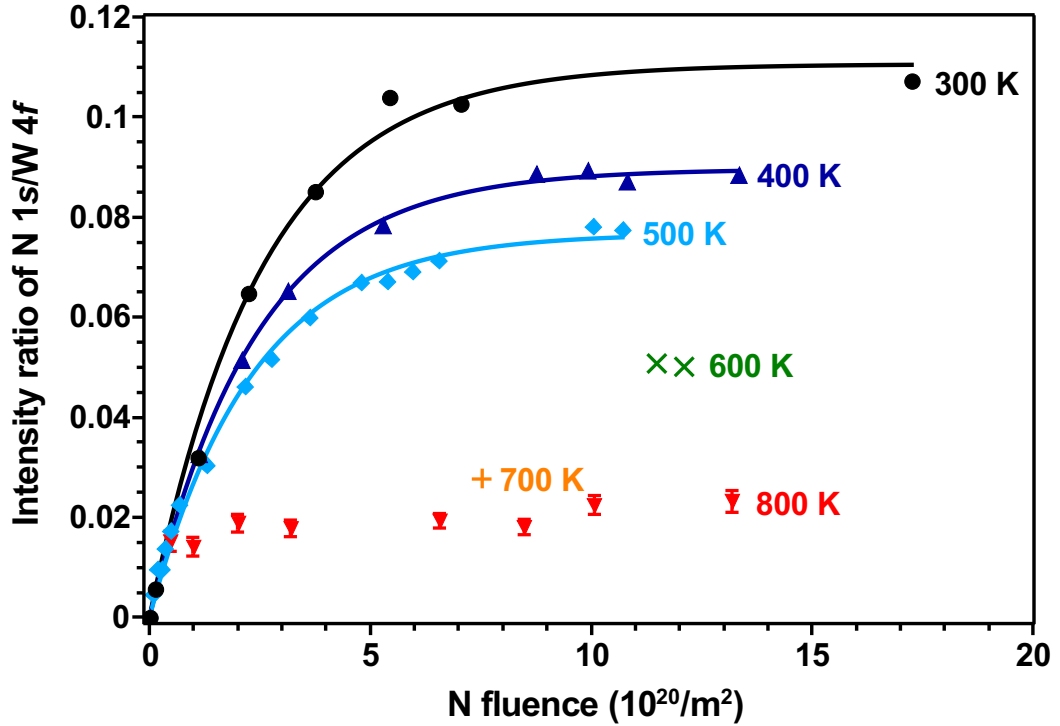


Figure 5.3: N implantation in W at different temperatures. The N level grows exponentially with the fluence until it saturates. The saturation level decreases linearly with increasing temperature, thus indicating a reduction of the total N amount in the surface.

The saturation levels for the 600 K and 700 K measurements originate from an implantation where the temperature was stepwise increased (see appendix A.1). Therefore, no fluence series is available.

The three fluence series at low temperatures follow the exponential growth

$$y = A \left( 1 - e^{-\frac{x}{t}} \right), \quad (5.1)$$

where  $y$  represents the intensity ratios and  $x$  the fluence. The saturation level  $A$  and the time constant  $t$  were determined by a least-square fit for the three series.

Temperature (K)	Saturation level $A$ (a.u.)	Time constant $t$ (a.u.)
300	0.11	2.5
400	0.089	2.4
500	0.076	2.3
600	0.051	-
700	0.029	-
800	0.023	-

Table 5.1: Saturation level  $A$  and time constant  $t$  for N implantation series at different temperatures.

They are summarized in table 5.1. For completeness, the saturation level of the three implantation measurements at higher temperature are also shown there.

For the data of the implantation at 800 K, the fitting approach was not pursued. As can be seen in figure 5.3, the data has an offset in y-direction and the intensity ratio increases only slightly. Evaluation of the raw data revealed, that the N level in the tungsten sample was already increased before implantation was started. This increased N level was probably caused by a nitrogen contaminated argon beam which was used to clean the sample surface for the experiment. For this reason, the first acquired XPS spectra are not shown.

It is notable that the time constant decreases only slightly with increasing temperature. In contrast, the saturation level decreases linearly with increasing temperature (see figure 5.4); by a factor of 4.8 between the implantation at 300 K and 800 K. This means that a thermally activated N loss occurs during implantation. Whether the nitrogen is lost to the surface or it diffuses into the depth of the sample, out of the XPS information depth, was addressed in the next step.

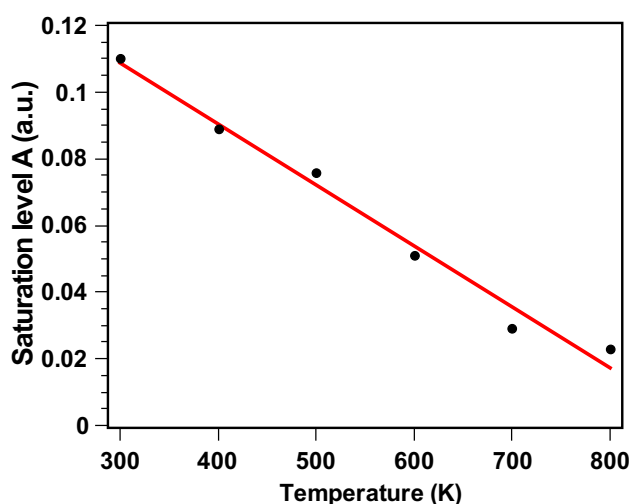


Figure 5.4: Linear decrease of the N saturation level with the implantation temperature; the blue dots show the extracted values for the saturation level  $A$  and the red line is a linear fit to these values.

For this purpose, sputter depth profiles were acquired which are presented in figure 5.5. Depending on the implantation temperature, the curves start at different levels but have the same decrease rate. This can be explained by a different N concentration in the sample surface.

All three depth profiles were performed at 300 K to minimize the N loss due to radiation enhanced diffusion (see section 2.3) [25]. Only three data points are shown from the depth profile of the 800 K implantation. At lower intensity ratios, the nitrogen contamination in the argon beam became dominant again<sup>9</sup>.

For the better understanding of the curve shape in the figure, forward calculations for two step profiles (see figure 5.6) were performed. The N concentration is given by the step profiles: nitrogen is present in the first 2 nm with 40 % and 20 %. The calculated XPS intensity ratios show the same behavior as the measured depth profiles for different implantation temperatures. This means that with increasing implantation temperature, the nitrogen concentration in the implantation range drops. This result also implies, that there is no enhanced diffusion of nitrogen towards the deeper layers of the tungsten sample.

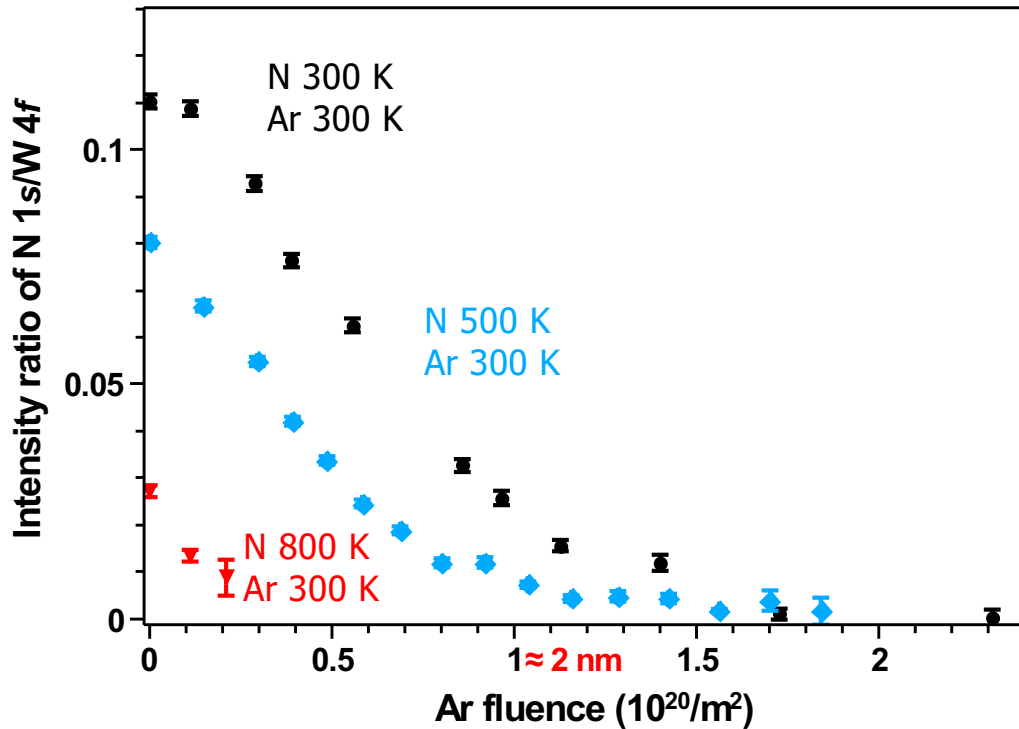


Figure 5.5: Depth profiles, measured at 300 K for implantation temperatures of 300, 500 and 800 K. The error bars indicate the statistical error. With increasing implantation temperature, the N concentration decreases, resulting in the shown depth profiles. Diffusion of nitrogen into the depth is not observed.

<sup>9</sup>The argon gas in the ion source was exchanged after its contamination was observed. Subsequent measurements confirmed that the argon beam was clean after the exchange.

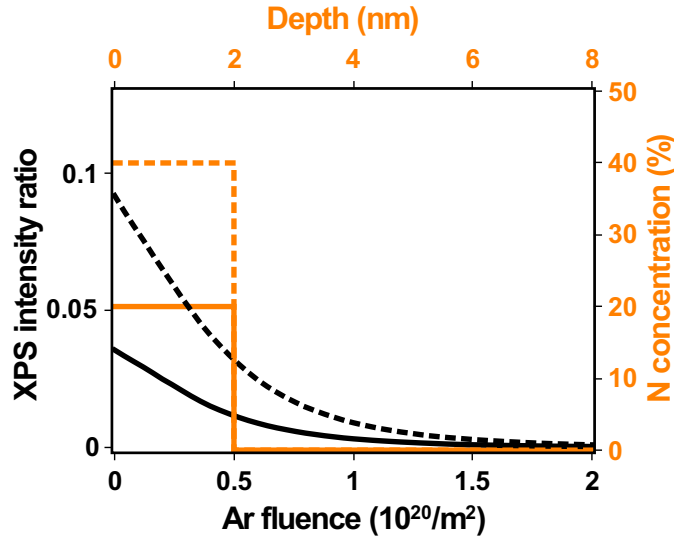


Figure 5.6: Forward calculations (black) for two N concentration step profiles (orange). The dashed line is analogous to a low temperature implantation, while the solid line to a higher temperature implantation.

### 5.3 Erosion of Tungsten Nitride

In the next two experiments, the temperature dependence of the N erosion was investigated. Figure 5.7 shows the measurement, in which WN was eroded by impinging N ions. Despite a permanent N supply, the N level decreases at elevated temperature. This shows, that the ion irradiation causes an enhanced N loss to the surface at elevated temperature.

Nitrogen was implanted into tungsten at 400 K until saturation. Subsequently, the sample was heated to 600 K and later to 700 K under continuous nitrogen irradiation. Despite a permanent N supply, the N level decreases at elevated temperature until a new equilibrium state is reached. The observed equilibrium levels are comparable to the saturation levels obtained from the implantation at 600 K and 700 K (see figure 5.3).

In the second erosion experiment, argon ions were employed, since they do not chemically interact with the WN system. The experimental data reveals, that the N erosion rate at 800 K is increased by a factor of two (violet dashed line in figure 5.8) compared to the N erosion rate at 300 K.

In this experiment, nitrogen was again implanted at 300 K until the N level saturated. Afterward, the WN sample was heated to 800 K and bombarded with Ar ions at elevated temperature. The corresponding XPS data points are shown as violet triangles in figure 5.8. The black circles represent the XPS intensity ratios for argon bombardment at 300 K. The lower start level of the high temperature measurement is probably due to adsorbed residual gas during annealing. The raw data reveals a carbon and oxygen contamination of circa 5 atomic percent for each component.

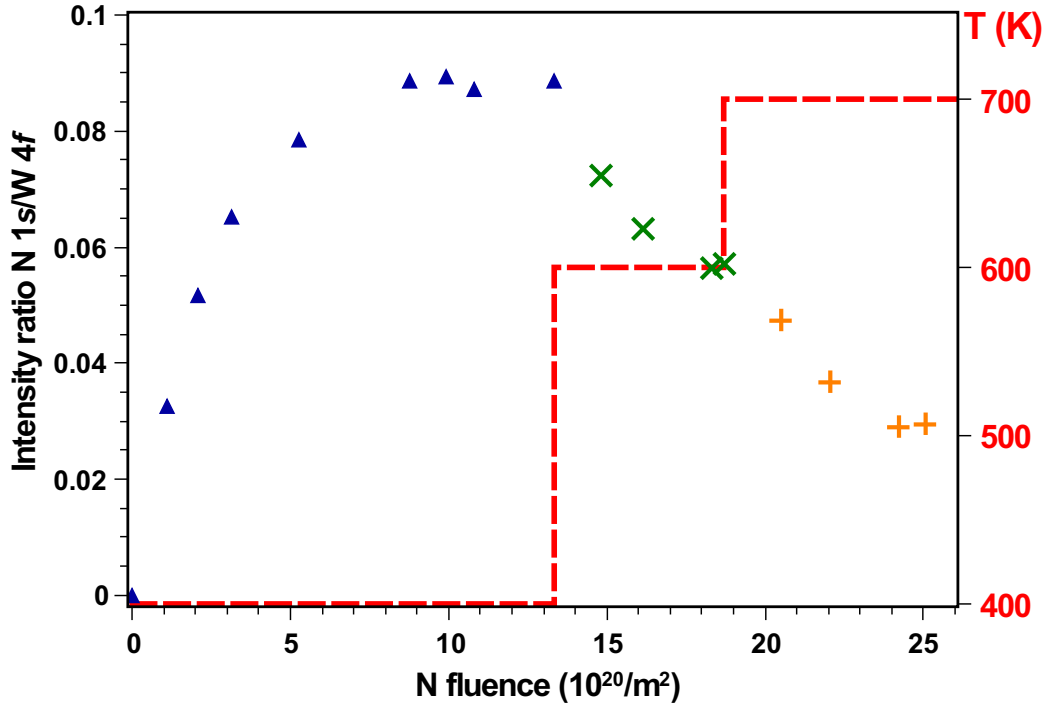


Figure 5.7: WN erosion by N ions. Despite the permanent nitrogen supply, the N content in the surface decreases at elevated temperature. This demonstrates, that the N loss to the surface only emerges during ion irradiation. The red dashed line indicates the temperature profile.

An explanation for the increased erosion at 800 K could be thermal diffusion. If 900 K would be reached on the sample surface, the WN phase would become unstable and decompose, thus the nitrogen would diffuse back to the surface. This additional heat for the temperature increase has to be supplied by the incoming argon ions. The heat flow  $\dot{Q}$  of the 1 keV Ar ions was experimentally determined to  $\dot{Q} = 10.6$  W. The heat flow which is needed to increase the temperature by  $\Delta T = 100$  K on the sample surface can be estimated via:

$$\dot{Q} = \kappa \frac{\Delta T}{d}, \quad (5.2)$$

with  $\kappa$ , the thermal conductivity and  $d$ , the sample thickness. For the tungsten samples with a thickness of 1 mm and  $\kappa = 170$  W/mK, this would mean, that a heat flow of approximately 17 MW is needed. Consequently, additional heat supply by the ion beam can be excluded and pure thermal diffusion does not account for the increased erosion.

The enhanced N erosion might be explained, if the sputter yield of argon on WN is increased at higher implantation temperatures. However, according to [14], the sputter yield in the range of 300 K to 800 K should be temperature independent.

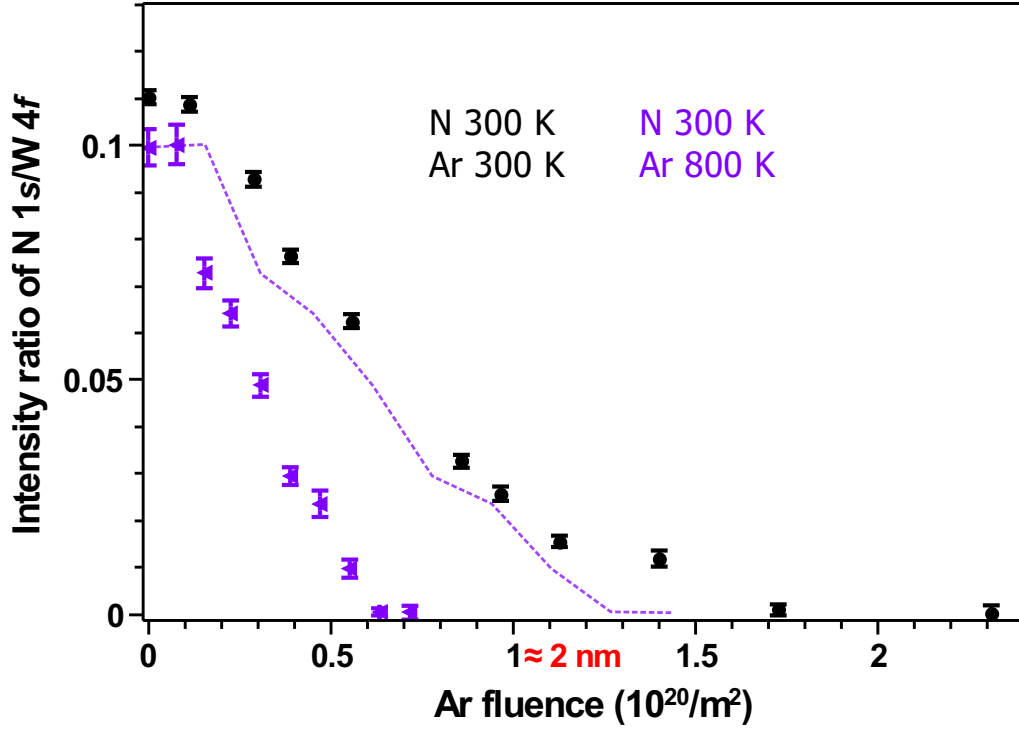


Figure 5.8: Measurements of the N erosion by argon sputtering at 300 K (black circles) and at 800 K (violet data points); The violet dashed line is a dilation of the x-values of the measured data. It shows, that the erosion at 800 K is about two times larger than at 300 K.

A third explanation for the increased erosion is radiation enhanced diffusion. As mentioned in section 2.3, ion irradiation causes additional vacancy-interstitial defects in the surface. The nitrogen atoms could be mobilized via the newly created defects, diffuse to the surface and leave it as  $\text{N}_2$  molecules. The nitrogen is, however, located in the interstices of the tungsten matrix. First of all, it needs energy to leave its octahedral or tetrahedral site, to diffuse out from the sample. In the next section, it is addressed, whether the enhanced N loss to the surface can be caused by vacancy diffusion.

## 5.4 Activation Enthalpy Calculation

To get an idea of the dimensions of the unknown nitrogen loss process, the same ansatz as for diffusive processes (see section 2.3) was made. The “effusive” nitrogen flux to the surface,  $\Gamma$ , is proportional to the gradient of the nitrogen particle density. Hence, Fick’s first law in one dimension can be used to calculate the proportionality factor  $D(T)$  according:

$$\Gamma(T) = D(T) \frac{dn(T)}{dx}. \quad (5.3)$$

At 300 K, WN is stable and the particle density of nitrogen  $n_N(300 \text{ K})$  is  $4.5 \times 10^{28} \text{ m}^{-3}$  [39]. Assuming that this N atom density of stoichiometric WN is reached for the 300 K implantation, the ratio of the sensitivity factors for N and W can be calculated. Using equation (3.10), the following is obtained:

$$\frac{n_N(300 \text{ K})}{n_{\text{WN}}} = \frac{\frac{I_N(300 \text{ K})}{I_N^\infty}}{\frac{I_N(300 \text{ K})}{I_N^\infty} + \frac{I_W(300 \text{ K})}{I_W^\infty}}. \quad (5.4)$$

Since

$$\frac{n_N(300 \text{ K})}{n_{\text{WN}}} = \frac{1}{2},$$

the ratio of the sensitivity factors equals to:

$$\frac{I_N^\infty}{I_W^\infty} = \frac{I_N}{I_W}(300 \text{ K}).$$

The nitrogen density  $n_N(T)$  for a temperature  $T$  higher than 300 K can be calculated from the measured N saturation level and the assumption that  $n_{\text{WN}}$  is independent of the temperature as follows:

$$n_N(T) = \frac{\frac{I_N(T)}{I_W(T)}}{\frac{I_N(T)}{I_W(T)} + \frac{I_N(300 \text{ K})}{I_W(300 \text{ K})}} n_{\text{WN}} \quad (5.5)$$

where  $\frac{I_N}{I_W}(T)$  is the measured intensity ratio at a specific temperature  $T$ .

The gradient of  $n_N$  can be approximated by the ratio of the nitrogen density and the implantation depth  $d$  of the N ions, i.e.  $\frac{dn_N(T)}{dx} \approx n_N/d$ . The implantation depth is obtained from SDTrimSP simulations and it is approximately 1.5 nm for the 300 eV implantation (see figure 2.2).

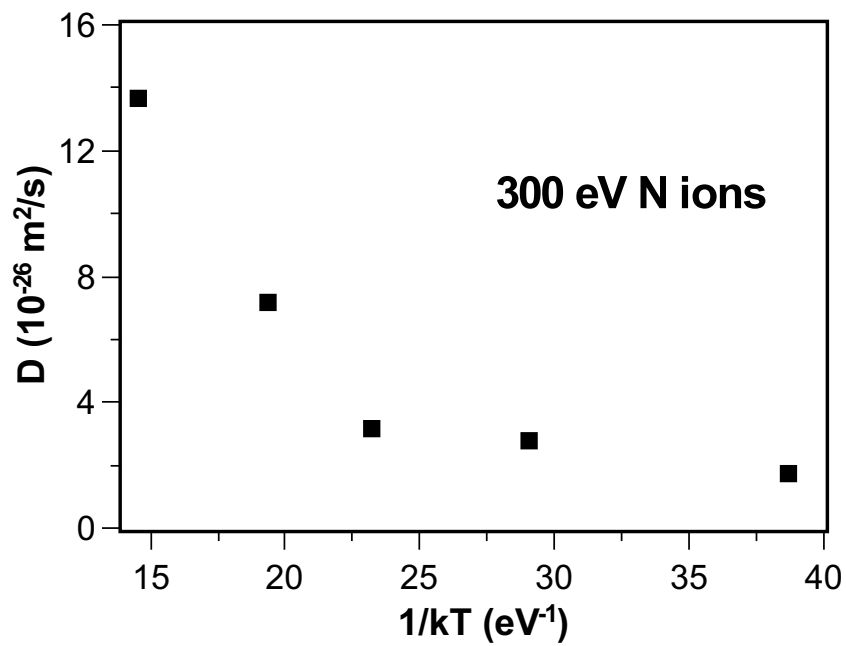
The effusive flux back to the surface,  $\Gamma(T)$ , can be extracted from the steady state condition, namely, that the incoming flux must be balanced by the outgoing flux:

$$\Gamma_{\text{in}} = \Gamma_{\text{out}} = \Gamma_{\text{refl}} + \Gamma_{\text{sp}} + \Gamma(T). \quad (5.6)$$

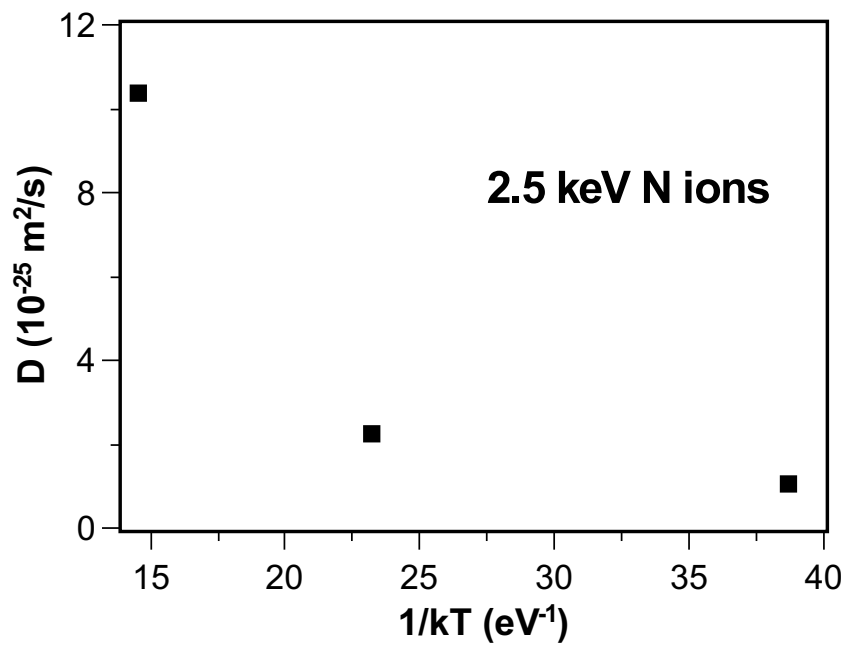
The outgoing flux consists of the effusive part,  $\Gamma(T)$ , the flux of ions which are reflected at the surface,  $\Gamma_{\text{refl}}$ , and the flux of sputtered N atoms,  $\Gamma_{\text{sp}}$ . The latter two can be calculated from the reflection and the sputter yield, which are provided by SDTrimSP simulations. By assuming that the sputter yield is proportional to the N particle density, as suggested in [40],  $\Gamma_{\text{sp}}$  can be calculated from XPS intensity ratios for  $T > 300 \text{ K}$ . The total incoming flux,  $\Gamma_{\text{in}}$ , is obtained by measuring the current on the sample.

$D(T)$  was determined for the implantation with 300 eV N ions and for the implantation with 2.5 keV N ions from [12]. The values are presented in figure 5.9.  $D(T)$  shows an Arrhenius-like temperature dependence (cf. equation (2.5)).

Figure 5.10 shows  $D(T)$  in an Arrhenius plot. The slope of the linear fit to the data points gives the activation enthalpy  $\Delta H$ . Its value for the 300 eV N implantation is 0.082 eV and 0.088 eV for the 2.5 keV N implantation. These values were calculated by means of many assumptions and should therefore be seen as rough estimates.

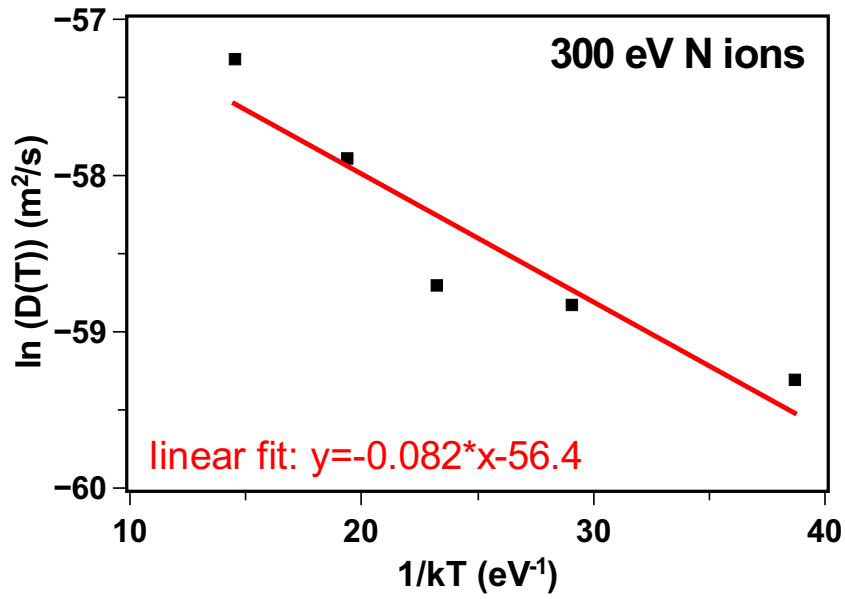


(a)

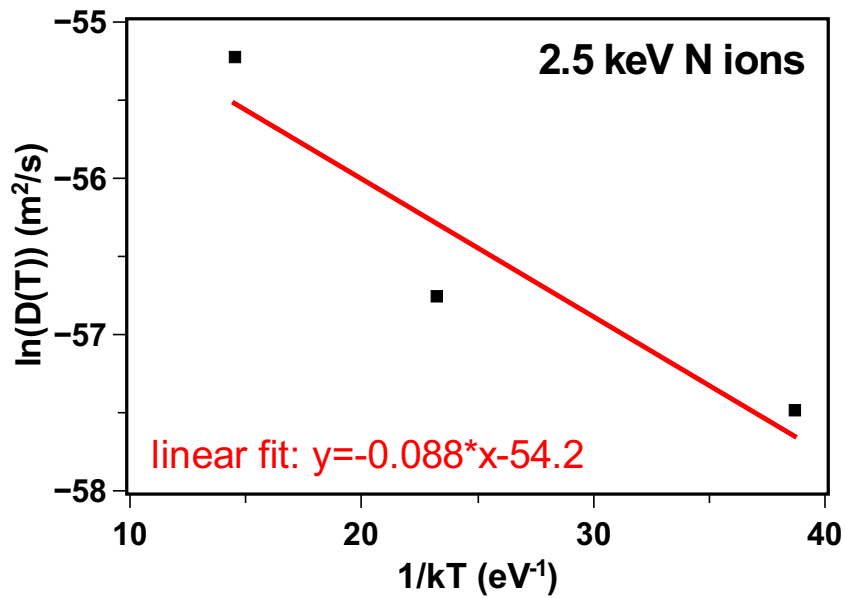


(b)

Figure 5.9:  $D(T)$ , calculated in the range 300 K to 800 K for the two implantation series with 300 eV and 2.5 keV N ions.



(a)



(b)

Figure 5.10: Arrhenius plot for the two implantation series with 300 eV and 2.5 keV N ions.  $\ln D(T)$  is plotted for different temperatures (black squares). The slope of the linear fit (red line) to the data points is the negative activation enthalpy  $\Delta H$  and the y-intercept gives  $\ln D_0$ . The value for  $D_0$  is lower for the 2.5 keV implantation, but the activation enthalpy is approximately the same.

The activation enthalpy for N diffusion in W at 900 K is 2.32 eV [5]. This value is significantly higher than the determined  $\Delta H$  from the N implantation. This difference confirms the observation that pure thermal diffusion does not account for the nitrogen loss up to 800 K. A proposed explanation for the increased N loss is radiation enhanced diffusion of nitrogen by vacancy migration. According to [6], the vacancy migration enthalpy in tungsten is 1.70 eV. This value is 20 times higher than the calculated activation enthalpies of the N loss. Hence, radiation enhanced diffusion by vacancy migration can be excluded as well. Another process or other created defects account for the nitrogen loss. The mechanism is still unclear but should be addressed in future experiments.

# Chapter 6

## Conclusion

### 6.1 Summary

In this thesis, the tungsten nitride (WN) formation and its erosion were studied by means of X-ray photoelectron spectroscopy (XPS). Nitrogen (N) was implanted into tungsten (W) under ultra-high vacuum conditions using a Wien filtered ion source. The N depth distribution and the N erosion were studied by bombarding the sample with argon (Ar) ions. To follow the surface evolution, XPS spectra were acquired alternating to the ion bombardment.

Previous implantation experiments with 2.5 keV N ions showed that the WN phase becomes unstable only above 900 K [4]. However, a phase change was expected already at 600 K from thermodynamic calculations [39]. Additional results were that the N level decreases with implantation temperature in the range 300 K to 800 K [4]. Accumulation and loss of N in this temperature range were further investigated in the scope of this work. For the implantation measurements, N ions of 300 eV kinetic energy were used. N ions of this energy are implanted until 2.5 nm depth. This lays in the range of the XPS information depth.

In the first experiment, a tungsten sample was implanted at 300 K with the N ions, until saturation was reached. Subsequently, the sample was heated to 800 K and held at this temperature for 5 h. The acquired intensity ratios of N and W scatter, but show no systematic loss of N. The scatter is attributed to re-adsorbed gas molecules. This indicates that the WN phase is stable at 800 K on a time scale of several hours.

For a more detailed evaluation, a sputter depth profile of the annealed sample was measured. It was compared to the depth profile of a N implantation at 300 K without annealing and to the calculated XPS profile from an implantation simulation with 300 eV N ions at “0 K”. All three profiles are in good agreement and show the same behavior with depth. From this, it can be deduced that a temperature increase up to 800 K does not change the N content in W.

The results look different when nitrogen is implanted into tungsten at elevated temperatures. The N saturation level ( $A$ ) decreases linearly with increasing temperature. The fluence series of the implantation at 300 K, 400 K and 500 K follow an

exponential growth which has the form of

$$y = A \left( 1 - e^{-\frac{x}{t}} \right),$$

where the time constant  $t$  decreases only slightly with increasing temperature.

Argon sputter depth profiles for the different implantation experiments were performed at 300 K. A comparison with forward calculations from two different step profiles shows that the behavior of the experimental intensity ratios could be explained by the same shape of the N depth distribution but varying concentration. The conclusion is that the N retention in tungsten decreases with increasing temperature. The depth profile also reveals that the N level is not decreased due to diffusion of N to larger depths and thus out of the sampling range of XPS.

In the first WN erosion experiment, a WN surface was bombarded with N ions. While the sample temperature was increased during ion bombardment, the N level dropped. The bombardment of tungsten nitride with argon at 800 K increased the N erosion by a factor of two compared to the argon bombardment at 300 K. A possible explanation for the increased N loss is enhanced diffusion through crystal defects, created by the ion irradiation.

Calculations using the experimental data show that the temperature dependence of the N loss process follows an Arrhenius relation. The activation enthalpy  $\Delta H$  was found to be 0.082 eV for the implantation of 300 eV N ions and 0.088 eV for the 2.5 keV N implantation from [4]. These values agree within their uncertainties and are significantly lower than the activation enthalpy for thermal diffusion of N in W at 900 K or the vacancy migration enthalpy in tungsten. This means that neither thermal diffusion nor radiation enhanced diffusion by vacancy migration can solely account for the loss of nitrogen from tungsten at elevated temperature.

The processes which occur in a WN system in the temperature range from 300 K to 800 K, when N ions of 300 eV are implanted in W, are summarized in figure 6.1. It was found, that a temperature dependent loss mechanism occurs which is caused by ion irradiation. Since the underlying mechanism is not fully understood, this process needs further investigation.

## 6.2 Outlook

So far, the only plausible explanation for the thermally activated N loss during implantation and the enhanced N erosion at elevated temperature is mobilization of the nitrogen via defects, created by the ion irradiation.

As the next step, WN erosion experiments with different ions or with more energetic Ar ions should be performed. The penetration depth of the ions increases with their kinetic energy. Defects are created deeper in the sample than the implantation depth of the 300 eV N ions. The N loss process, which is increased by the created defects, should then appear in larger depth and change the N depth distribution in the W sample.

Another approach to consider is to use a non-perturbative depth profiling method to investigate the variation of the N depth distribution with varying temperature.

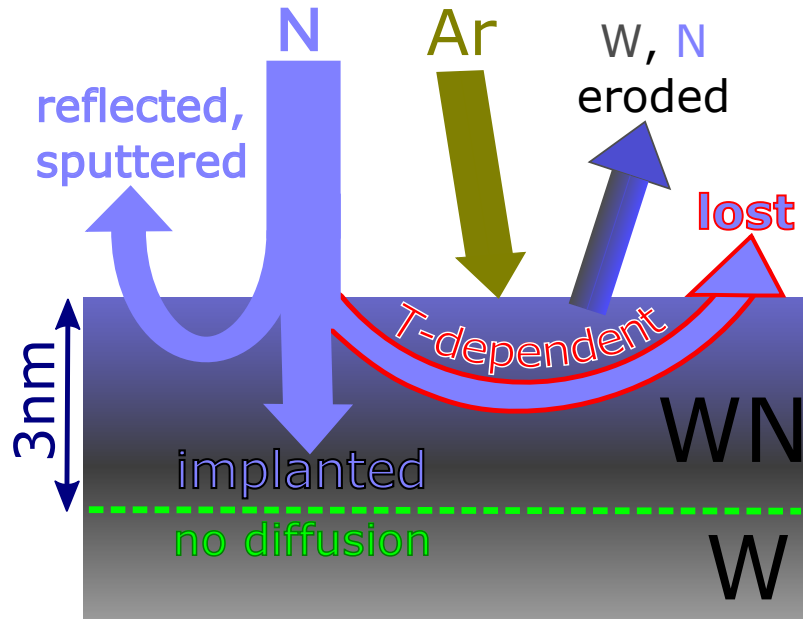
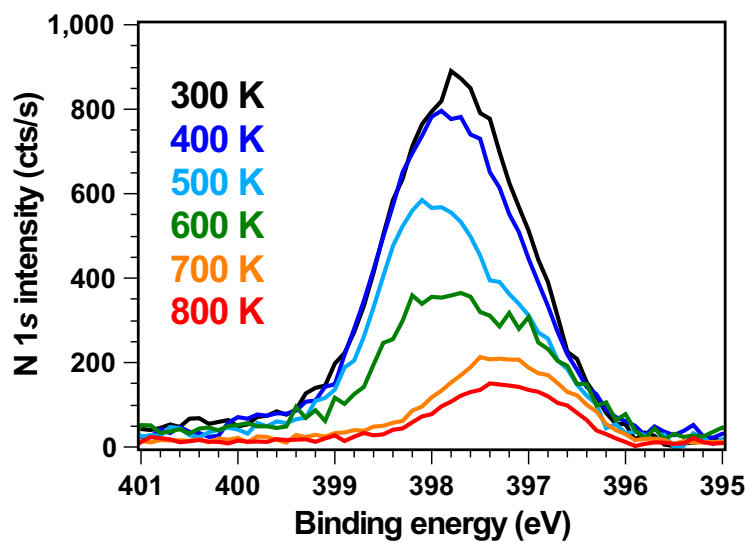


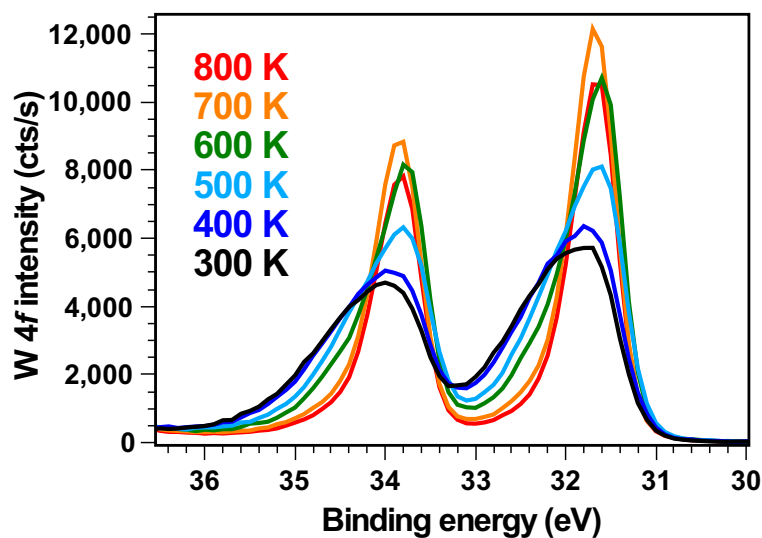
Figure 6.1: Illustration of the processes which occur in the investigated WN system. Figure adapted from [12].

The most practicable method is angle-resolved depth profiling: The sample gets tilted with respect to the analyzer. The detected electrons leave the sample under the angle  $\theta$  and the sampling depth is decreased by a factor of  $\cos \theta$  [23]. Before this method can be employed, the rotation axis of the specimen holder with respect to the analyzer has to be determined carefully.

High resolution measurements of the the N  $1s$  and the W  $4f$  peaks were performed during the experiment shown in appendix A.1. The measurements of the N  $1s$  peak can be seen in figure 6.2a. They reveal, that at 600 K the electronic structure starts to change. A second peak at higher binding energy appears with decreasing temperature. The W  $4f$  peak (see figure 6.2b) shifts also to higher binding energies and is broadened when the temperature is decreased. This demonstrates that more tungsten nitride is produced at lower temperatures. Whether these observations can be directly related to a change of the nitrogen location in the tungsten crystal is unclear. Therefore, more measurements are needed.



(a)



(b)

Figure 6.2: High resolution measurement of the N 1s peak (a) and the W 4f peak (b) in the temperature range from 300 to 800 K. The measurement of the N 1s peak reveals that at 600 K (green), a second component at slightly higher binding energy occurs. The W 4f peak also shifts to higher binding energies with lower temperature since more WN is formed.

# Appendix A

## Further Measurements

### A.1 Temperature Ramp

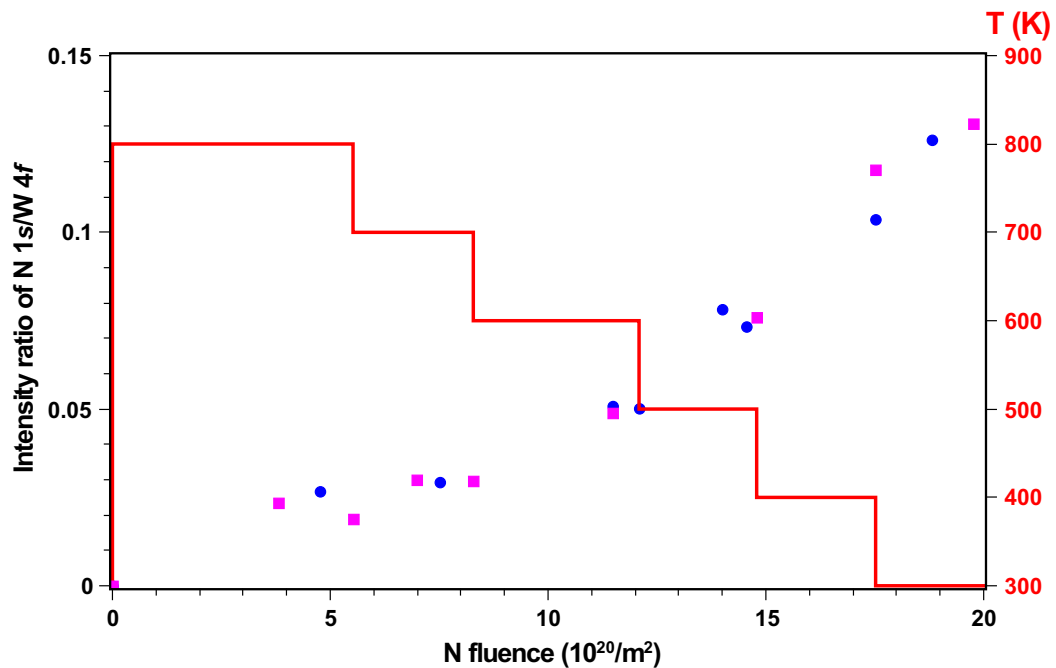


Figure A.1: N saturation levels during nitrogen implantation. The experiment started with N ion implantation at 800 K until saturation was reached. Then the temperature was decreased by 100 K and N implantation was started again until the N level saturated. This procedure was followed until 300 K. The blue circles were measured with a pass energy of 93.9 eV, magenta squares with 11.75 eV and the red line indicates the temperature profile.

In the experiment with the temperature ramp, the N saturation levels in the temperature range between 300 K and 800 K were determined (see figure A.1). The implantation was started at 800 K until the N level saturated. Then, the temperature

was decreased to 700 K and N implantation was continued until the new saturation level was reached. This happened at a N fluence of approximately  $7.5 \times 10^{20} \text{ m}^{-2}$ . The temperature was further decreased by 100 K and N was implanted again until it saturated. The N fluence added up to ca.  $11 \times 10^{20} \text{ m}^{-2}$ . The procedure was continued until saturation at 300 K was reached. Data was acquired with a pass energy of 93.9 eV (blue dots) and 11.75 eV (magenta squares).

## A.2 Fluence Dependence

During a N implantation at 300 K, high resolution measurements at different fluence were acquired (see figure A.2). The spectra show a shift to lower binding energies at higher fluence, which means that the electronic structure of the nitrogen changes during the implantation process. This also indicates that the nitrogen is implanted in different chemical environments.

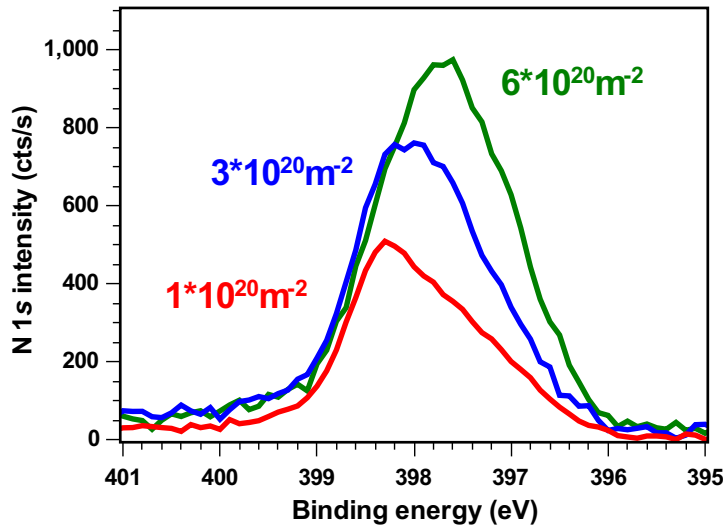


Figure A.2: High resolution measurement of the nitrogen peak. The peak shifts to lower binding energies with the N fluence (written in the figure), thus indicating that the chemical state of the formed tungsten nitride changes.

# Bibliography

- [1] ITER. *Divertor*. URL: <https://www.iter.org/mach/divertor>.
- [2] Ralph Dux. *Plasmaphysik und Fusionsforschung - Teil II: Fusionsforschung*. Lecture notes. 2002.
- [3] A. Kallenbach, M. Balden, et al. “Plasma surface interactions in impurity seeded plasmas”. In: *Journal of Nuclear Materials* 415.1, Supplement (2011). Proceedings of the 19th International Conference on Plasma-Surface Interactions in Controlled Fusion, S19–S26. ISSN: 0022-3115. DOI: <http://dx.doi.org/10.1016/j.jnucmat.2010.11.105>.
- [4] G. Meisl, K., et al. “Implantation and erosion of nitrogen in tungsten”. In: *New Journal of Physics* 16.9 (2014), page 093018. URL: <http://stacks.iop.org/1367-2630/16/i=9/a=093018>.
- [5] J. Keinonen, J. Räisänen, et al. “Diffusion of nitrogen in ion-implanted chromium and tungsten”. In: *Applied Physics A* 35.4 (), pages 227–232. ISSN: 1432-0630. DOI: [10.1007/BF00617172](https://doi.org/10.1007/BF00617172).
- [6] A. Satta, F. Willaime, et al. “Vacancy self-diffusion parameters in tungsten: Finite electron-temperature LDA calculations”. In: *Phys. Rev. B* 57 (18 May 1998), pages 11184–11192. DOI: [10.1103/PhysRevB.57.11184](https://doi.org/10.1103/PhysRevB.57.11184).
- [7] Susan Boenke. *Entstehung und Entwicklung des Max-Planck-Instituts für Plasmaphysik, 1955-1971*. Campus Verlag, 1991.
- [8] George Wallerstein, Icko Iben, et al. “Synthesis of the elements in stars: forty years of progress”. In: *Rev. Mod. Phys.* 69 (4 Oct. 1997), pages 995–1084. DOI: [10.1103/RevModPhys.69.995](https://doi.org/10.1103/RevModPhys.69.995).
- [9] Ulrich Stroth. *Plasmaphysik – Phänomene, Grundlagen, Anwendungen*. Vieweg + Teubner Verlag, 2011. ISBN: 9783834816153. DOI: [10.1007/978-3-8348-8326-1](https://doi.org/10.1007/978-3-8348-8326-1).
- [10] Olaf Encke. “Wechselwirkung von Stickstoff- und Deuterium-Ionen mit Wolfram”. Master’s thesis. Universität Ulm, 2014.
- [11] G. Federici, C.H. Skinner, et al. “Plasma-material interactions in current tokamaks and their implications for next step fusion reactors”. In: *Nuclear Fusion* 41.12 (2001), page 1967. URL: <http://stacks.iop.org/0029-5515/41/i=12/a=218>.
- [12] Gerd Meisl. “Nitrogen Migration in ASDEX Upgrade”. PhD thesis. Technische Universität München, 2014.

- [13] A. Kallenbach, R. Dux, et al. “Divertor power load feedback with nitrogen seeding in ASDEX Upgrade”. In: *Plasma Physics and Controlled Fusion* 52.5 (2010), page 055002. URL: <http://stacks.iop.org/0741-3335/52/i=5/a=055002>.
- [14] Klaus Schmid. “Untersuchung der Temperaturabhängigkeit der Erosion von Wolfram durch Kohlenstoff”. PhD thesis. Universität Bayreuth, 2001.
- [15] R.A. Langley, J. Bohdansky, et al. “Data Compendium for Plasma-Surface Interactions”. In: *Nuclear Fusion* 24.S1 (1984), S9. URL: <http://stacks.iop.org/0029-5515/24/i=S1/a=001>.
- [16] A. Mutzke, R. Schneider, et al. *SDTrimSP Version 5.00*. IPP-Report 17/12, Max-Planck-Institut für Plasmaphysik, 2009. URL: <http://edoc.mpg.de/display.epl?mode=doc&id=434557&col=33&grp=1311#cb>.
- [17] Gerd Meisl. Private communication.
- [18] Theodor Heumann. *Diffusion in Metallen – Grundlagen, Theorie, Vorgänge in Reinmetallen und Legierungen*. Springer-Verlag, 1992.
- [19] Helmut Mehrer. *Diffusion in Solids – Fundamentals, Methods, Materials, Diffusion-Controlled Processes*. Springer-Verlag, 2007. DOI: [10.1007/978-3-540-71488-0](https://doi.org/10.1007/978-3-540-71488-0).
- [20] Todd R. Allen and Gary S. Was. “Radiation Effects in Solids”. In: edited by Kurt E. Sickafus, Eugene A. Kotomin, et al. Springer Netherlands, 2007. Chapter *Radiation-enhanced diffusion and radiation-induced segregation*, pages 123–151. ISBN: 9781402052958. DOI: [10.1007/978-1-4020-5295-8\\_6](https://doi.org/10.1007/978-1-4020-5295-8_6).
- [21] Wolfgang Bolse. “Ion-beam induced atomic transport through bi-layer interfaces of low- and medium-Z metals and their nitrides”. In: *Materials Science and Engineering: R: Reports* 12.2 (1994), pages vii–121. ISSN: 0927-796X. DOI: [http://dx.doi.org/10.1016/0927-796X\(94\)90001-9](http://dx.doi.org/10.1016/0927-796X(94)90001-9).
- [22] Wikipedia. *Photoelektrischer Effekt*. URL: [https://de.wikipedia.org/wiki/Photoelektrischer\\_Effekt](https://de.wikipedia.org/wiki/Photoelektrischer_Effekt).
- [23] John C. Vickerman. *Surface Analysis – The Principal Techniques*. John Wiley & Sons, Ltd, 2000. ISBN: 9780470721582. DOI: [10.1002/9780470721582.ch1](https://doi.org/10.1002/9780470721582.ch1).
- [24] Wikipedia. *Photoelektronenspektroskopie*. URL: [https://de.wikipedia.org/wiki/Photoelektronenspektroskopie#mediaviewer/Datei:XPS\\_-\\_Energy\\_levels\\_\(schematic\)\\_DE.svg](https://de.wikipedia.org/wiki/Photoelektronenspektroskopie#mediaviewer/Datei:XPS_-_Energy_levels_(schematic)_DE.svg).
- [25] D. Briggs and J.T. Grant. *Surface Analysis by Auger and X-ray Photoelectron Spectroscopy*. SurfaceSpectra, 2003. ISBN: 9781901019049. URL: <https://books.google.de/books?id=HY6PQgAACAAJ>.
- [26] Wikipedia. *Augereffekt*. URL: [https://de.wikipedia.org/wiki/Datei:Atom\\_model\\_for\\_Auger\\_process\\_DE.svg](https://de.wikipedia.org/wiki/Datei:Atom_model_for_Auger_process_DE.svg).
- [27] János Végh. “The Shirley background revised”. In: *Journal of Electron Spectroscopy and Related Phenomena* 151.3 (2006), pages 159–164. ISSN: 0368-2048. DOI: <http://dx.doi.org/10.1016/j.elspec.2005.12.002>.

- [28] M. P. Seah and I. S. Gilmore. “Quantitative x-ray photoelectron spectroscopy: Quadrupole effects, shake-up, Shirley background, and relative sensitivity factors from a database of true x-ray photoelectron spectra”. In: *Phys. Rev. B* 73 (17 May 2006), page 174113. DOI: [10.1103/PhysRevB.73.174113](https://doi.org/10.1103/PhysRevB.73.174113).
- [29] Jill Chastain and Roger C. King, editors. *Handbook of X-ray Photoelectron Spectroscopy*. Physical Electronics, Inc., 1995. ISBN: 096481241X.
- [30] Walter Umraht. *Vacuum Technology - Grundlagen der Vakuumtechnik*. May 2002.
- [31] John F. Watts and John Wolstenholme. *An Introduction to Surface Analysis by XPS and AES*. John Wiley & Sons, Ltd, 2005. ISBN: 9780470867938. DOI: [10.1002/0470867930.fmatter](https://doi.org/10.1002/0470867930.fmatter).
- [32] Physical Electronics Division. *Model 10-360 Precision Energy Analyzer*. Technical Manual.
- [33] SPECS GmbH. *Ion Source IQE 12/38*. Operation Manual, 2008.
- [34] SPECS GmbH. *Wien Mass Filter WF-IQE*. Operation Manual, 2007.
- [35] Gabriele Matern. Private communication.
- [36] G.F. Matthews. “Material migration in divertor tokamaks”. In: *Journal of Nuclear Materials* 337–339 (2005). PSI-16, pages 1–9. ISSN: 0022-3115. DOI: <http://dx.doi.org/10.1016/j.jnucmat.2004.10.075>.
- [37] Physical Electronics Division. *Model 10-420 Toroidal Monochromator*. Technical Manual.
- [38] Udo von Toussaint. Private communication.
- [39] K. Schmid, A. Manhard, et al. “Interaction of nitrogen plasmas with tungsten”. In: *Nuclear Fusion* 50.2 (2010), page 025006. URL: <http://stacks.iop.org/0029-5515/50/i=2/a=025006>.
- [40] K. Schmid, M. Reinelt, et al. “An integrated model of impurity migration and wall composition dynamics for tokamaks”. In: *Journal of Nuclear Materials* 415.1, Supplement (2011). Proceedings of the 19th International Conference on Plasma-Surface Interactions in Controlled Fusion, S284–S288. ISSN: 0022-3115. DOI: <http://dx.doi.org/10.1016/j.jnucmat.2011.01.105>.

# Acknowledgement

First of all, I want to thank PD Dr. Jörg Stober who awoke my interest in the field of plasma physics and nuclear fusion research. He got me into contact with the IPP and offered to supervise my thesis.

I also want to thank Prof. Dr. Ulrich Stroth for the opportunity to write my thesis at the E2M department and Dr. Marco Wischmeier for providing the topic.

I owe my special thanks to Gerd Meisl, the best tutor I can imagine. He not only introduced me to the experimental work but generally to the scientific methodology. He was always very helpful, especially when a component of the XPS device was broken, extremely patient in explaining the underlying physics of the experiment and he gave me good suggestions for the evaluation of the measurements as well as for my thesis.

I am also grateful to Dr. Wolfgang Jacob for his advices and grateful to all his group members. The weekly discussions at the round table were very fruitful concerning my own work and they also helped me to get a general understanding for problems emerging in fusion research. I would also like to take this opportunity to thank Till Höschen who, in particular, helped me to adjust the ion sources and I could always ask him, when questions concerning the XPS method emerged. My thanks also go to Udo von Touissant who not only wrote the program for calculating the statistical error of the measurements but also gave me advices in evaluating and presenting the obtained data. I thank Gabriele Matern for showing me how to prepare the tungsten samples.

I thank all the people who are not called by name here, but provided me an educative and enjoyable year at the IPP.

Other people who are not directly connected to the IPP, but still helped me to successfully finish this work are my friends, Tobias Pärri and Armin Shaukat. I am grateful that I could share my years of study with them. Even more, I want to thank my family for their support during my whole life. My parents are the ones who made it possible, that this master thesis could be written. Last but not least, I thank László Szűcs for proofreading my thesis and giving comments on it, which hopefully improve its understandability. Nevertheless, I thank him for many more things, especially for his persistence.